Applied Thermal Engineering 286 (2026) 129325

Contents lists available at ScienceDirect

Applied Thermal Engineering

journal homepage: www.elsevier.com/locate/ate

Research Paper

Additively manufactured phase change material heat sinks for satellite thermal management

Laryssa Sueza Raffa [a,*], Matt Ryall [b], Nick S. Bennett [a], Lee Clemon [a,c]

[a] School of Mechanical and Mechatronic Engineering, University of Technology Sydney, Ultimo, NSW 2007, Australia
[b] Mawson Rovers, Eveleigh, NSW 2015, Australia
[c] Mechanical Science and Engineering, The Grainger College of Engineering, University of Illinois Urbana-Champaign, Urbana, IL 61801, USA

ARTICLE INFO

Keywords:
Thermal management
Satellite electronics
Heat sink
Phase change material (PCM)
Triply periodic minimal surfaces (TPMS)
Additive manufacturing

ABSTRACT

Maintaining satellite electronics within their maximum allowable operating temperatures is crucial for long-term reliability, yet increasingly power-dense payloads and miniaturized satellites introduce severe challenges. To meet the demand for efficient thermal management, this study leverages advances in additive manufacturing and explores triply periodic minimal surface (TPMS) heat sinks with phase change material (PCM) for space use, a growing area but with limited research. As part of the design development of the University of Technology Sydney's payload Matilda, this work examined how geometry, material composition, and orientation influence the performance of PCM-based thermal management modules. Five heat sink designs were investigated: hollow, gyroid, I-graph-Wrapped Package-graph (IWP), swirl, and radial plane fins. The heat sinks were 3D-printed from titanium and stainless steel, filled with paraffin wax PCM, and tested under vacuum at two power levels. Key parameters such as internal surface area and mass were analysed. Results show that, although material thermal conductivity influences temperature, design-dependent factors such as total metallic mass and internal structure distribution dominate heat dissipation. The gyroid achieved the lowest temperatures, though at the cost of increased mass, while mass-normalized performance identified the IWP lattice and radial-finned designs as most efficient. A mass-matched comparison of these two revealed nearly identical performance despite 27% difference in internal surface area, underscoring the role of total mass and internal geometry distribution. Orientation and initial PCM position had minimal influence, with less than 4 °C variation. These findings demonstrate that thermal performance is heavily affected by material properties, total mass, and structure distribution, with geometric complexity offering secondary benefits, and orientation and PCM position yielding minimal returns.

1. Introduction

Ensuring stable temperatures of electronics is critical for system reliability and longevity. Elevated temperatures are responsible for nearly 50% of electronic failures [1], with failure rates that double every 10 °C increase [2]. In space, the absence of convective heat dissipation limits cooling options to conduction through spacecraft structures and radiation. CubeSats, which are small satellites with a standard form factor and size varying from 1U (100 x 100 x 100 mm) to 12U (12 times 1U cube size), have enabled significant advancements in academic research and technology demonstrations due to lower costs and shorter development times relative to typical commercial satellites [3]. The small form factor of CubeSats limits the area available for heat dissipation, making effective thermal management strategies essential, particularly for high-power electronics. Phase change material (PCM) based modules have gained attention as a promising solution to regulate temperatures. PCMs store and release a high amount of thermal energy relative to their mass due to their high latent heat capacity during phase change [4]. Their high energy density and ability to absorb and release energy based on temperature makes them particularly attractive for intermittent and cyclic heat loads [5,6]. Waste heat generated during electronics operation is absorbed by the high latent heat of fusion of PCMs, preventing electronics from exceeding safe operating temperatures. In periods of reduced power consumption, the stored thermal energy is gradually released during PCM solidification, resetting for the upcoming thermal cycle. The high energy density of PCMs is also advantageous to CubeSats as they promote a lightweight and compact solution for thermal management. However, most pure PCMs feature inherent low thermal conductivity, which can limit heat transfer and affect thermal performance [7]. Among them, organic PCMs such as paraffin waxes typically possess the lowest thermal

* Corresponding author.
E-mail address: laryssa.suezaraffa@uts.edu.au (L. Sueza Raffa).

https://doi.org/10.1016/j.applthermaleng.2025.129325
Received 3 October 2025; Received in revised form 12 November 2025; Accepted 29 November 2025
Available online 5 December 2025

Nomenclature

English symbols

A	Surface area (m^2)
C_p	Specific heat capacity (J/kg K)
H	Latent heat of fusion (J/kg)
h	Convection heat transfer coefficient (W/m^2K)
k	Thermal conductivity (W/m K)
L_1	Conduction path length (m)
m	Mass (kg)
$P_{heatsink}$	Power input on heat sink base surface (W)
P_{heater}	Heater power (W)
Q	Energy (J)
q	Heat rate (W)
R	Heater resistance (Ω)
T	Temperature (° C)
t	Time (s)
U	Voltage (V)
V	Volume (m^3)

Greek symbols

ϵ	Emissivity
λ	Liquid fraction
σ	Stefan–Boltzmann constant (5.67×10^{-8} W m^{-2} K^{-4})

Subscripts

out	Leaving a system
HS	Heat sink
PCM	Phase change material
top	Referent to the heat sink's top surface
$base$	Referent to the heat sink's base surface
$structure$	Referent to the heat sink's internal structure
$surface$	Referent to the heat sink's external surface
$void$	Referent to the heat sink's internal void
$overall$	Referent to the heat sink's overall external outline
∞	Surroundings
i	initial
f	final

conductivity, and inorganic PCMs exhibit slightly higher values, yet still significantly below those of metallic PCMs [4].

Extensive research has been done to explore distinct techniques to enhance heat transfer within the PCM, including the addition of fins, metal foams, and nano-encapsulation of PCMs, as reviewed by Maqbol et al. [8], and Bose and Amitham [9]. The use of fins as a heat transfer enhancement has demonstrated positive outcomes in electronics cooling terrestrially [10]. In addition, the effects of fin parameters in the performance of PCM-based finned heat sinks has been extensively reported in the literature, such as fin geometry [11] and fin height, thickness, and spacing [12]. Zhang et al. [13] provides a comprehensive review of fin designs for thermal energy storage. Advancements in additive manufacturing have enabled the fabrication of complex heat sink structures for thermal conductivity enhancement. While conventional heat sinks are limited to machined fins, or extruded structures, additively manufactured heat sinks can feature intricate lattice designs, including triply periodic minimal surfaces (TPMS) and porous metal matrices. TPMS metamaterials have been gaining popularity in the design of advanced heat sinks due to their high surface area to volume ratio, allowing for efficient heat dissipation while maintaining a lightweight structure. Several studies for terrestrial applications have demonstrated that TPMS heat sinks significantly improve the effective thermal conductivity of the PCM-based heat sink module, promoting effective heat transfer and uniform PCM melting. Qureshi et al. [14] conducted a numerical study on TPMS structures of same cell size and porosity under an applied temperature gradient. The study concluded that sheet-based TPMS designs, such as gyroid, IWP, and primitive, outperformed strut-based structures like Kelvin. They also found that the effective thermal conductivity is only associated with cell architecture, regardless of the surface area of the cell. Similarly, in an experimental study with gyroid, diamond and SchWarz TPMS lattices, Catchpole et al. [15] observed that thermal conductivity depended mainly on material properties and volume fraction, with slight geometric influence. The Schwarz primitive presented the highest conductivity, with larger cells showing higher conductivity. Gopalan et al. [16] analysed PCM-based heat sinks enhanced with square, diamond, and octahedral lattices and square and hexagonal honeycomb structures. The transient simulations compared the thermal performance of these structures against pure PCM, evaluating the effects of porosity, and configuration. The results indicate that, for the same porosity, all the configurations yielded similar thermal responses. Hence, the study concludes that the performance depends solely on effective thermal conductivity, regardless of enhancer type or configuration. The heat sinks with internal structures consistently outperformed pure PCM. Through numerical modelling validated with experimental testing, Arqam et al. [17] investigated a TPMS lattice heat sink and a finned heat sink under varying heat flux directions. Results show that the TPMS lattice improves heat transfer to PCM, by enabling more uniform PCM melting. While the radial fin design achieved 3 to 4 °C lower base temperatures under base-only heating, the TPMS geometry outperformed it in side-heating scenarios by keeping the walls 6 to 8 °C cooler, making it more suitable for multidirectional heat input applications.

PCM-based thermal management modules have gained increasing attention for space applications due to the miniaturization of satellite electronics and rising power densities. Sueza Raffa et al. [18] experimentally and numerically assessed the impact of PCM in metallic heat sinks operating in vacuum and atmospheric conditions. The results showed that vacuum operation led to 32.8% higher temperatures due to the lack of convective heat transfer. The presence of PCM reduced peak temperatures by 18.0 °C in vacuum and 12.3 °C in atmospheric conditions, nearly doubling operating time and enhancing thermal regulation. A limited number of studies have focused on optimizing heat sink designs to improve PCM thermal performance. Raj et al. [19] conducted a numerical study on the influence of fin geometry in heat sinks with solid–solid PCM for satellite avionics. After evaluating fin shape, thickness, and count, the results indicate that tapered triangular fins provided the best balance between thermal performance and weight reduction, compared to straight circular and square counterparts. Elshaer et al. [20] investigated the role of fin configurations in enhancing the thermal conductivity of RT 35 PCM in aluminium heat sinks for small satellite subsystems. Parallel, cross, and pin fins were numerically analysed and pin fins outperformed the other types. Among the pin fin geometries square, circular, and triangular, the latter exhibited the greatest peak temperature reduction. More fins improved heat dissipation at the expense of reduced PCM volume though. A numerical study of a vertical cylinder filled with PCM was conducted by Izgi [21]. The study compared the PCM cylinder with no fins under both gravity and microgravity and found that melting time increased by 39.3% relative to gravity. Fin thicknesses were compared under microgravity and it was concluded that, wider fins led to greater reduction in melting time compared to a heat sink without fins. Wang et al. [22] analysed heat conduction enhancements in a PCM-based tubular thermal storage unit for spacecraft through

Table 1
Representative studies of finned and TPMS PCM-based heat sinks and thermal storage modules for spacecraft applications.

Reference	Geometry	PCM	Conditions	Method	Main Findings
Raj et al. (2020) [19]	Square, triangular, circular fins	Perovskite (solid–solid PCM)	Vacuum	Numerical	Tapered triangular fins achieved best performance-to-weight ratio.
Elshaer et al. (2023) [20]	Pin, cross, and parallel fins	RT 35 (paraffin wax)	Vacuum, microgravity	Numerical	Pin fins lowered peak temperature most effectively.
Izgi (2023) [21]	Plane fins	RT-27 (paraffin wax)	Gravity vs microgravity	Numerical	Lower gravity slowed melting by 39% without fins; wider fins reduced melting time compared to finless design.
Wang et al. (2022) [22]	Fins, metal and graphite foams	RT 50 (paraffin wax)	Microgravity	Numerical	A hybrid 3% fins and 98% Cu foam found to be the best performer design.
Guo et al. (2021) [23]	TPMS lattice	n-tetradecane (paraffin wax)	Vacuum, gravity	Experimental	Achieved 13× conductivity increase vs. pure PCM.
Sueza Raffa et al. (2025) [18]	Fins	Sigma Aldrich 53–58 °C (paraffin wax)	Vacuum vs atmospheric, gravity	Experimental	PCM reduced peak temperature by 18 °C (vacuum) and 12 °C (atmospheric).
Baby and Balaji (2013) [24]	Metal foam	n-eicosane (paraffin wax)	Atmospheric, gravity	Experimental	Heat transfer performance was similar at 0°, 90°, and 180°.
Fok et al. (2010) [25]	Fins	n-eicosane (paraffin wax)	Atmospheric, gravity	Experimental	Phase change was minimally affected by orientation.

Table 2
Details of the heat sinks compared in the experiment. All heat sinks were filled with 6.0 g of PCM.

Design	Material	Metal mass (g)	PCM mass (g)	$A_{structure}$ (mm^2)	$V_{void}/V_{overall}$	V_{PCM}/V_{void}
No TCE/hollow (P1)	Ti-6Al-4V	28.5	6.0	0	0.81	0.31
No TCE/hollow (P1)	SS316L	52.3	6.0	0	0.81	0.31
Gyroid cells (P2)	Ti-6Al-4V	67.2	6.0	18 913	0.56	0.50
Gyroid cells (P2)	SS316L	129.3	6.0	18 913	0.56	0.50
IWP lattice (P3)	Ti-6Al-4V	39.3	6.0	7226	0.66	0.38
IWP lattice (P3)	SS316L	73.9	6.0	7226	0.66	0.38
Swirl cells (P4)	Ti-6Al-4V	46.2	6.0	7334	0.61	0.41
Swirl cells (P4)	SS316L	86.8	6.0	7334	0.61	0.41
Radial plane fins (P5)	Ti-6Al-4V	35.7	6.0	5755	0.70	0.36
Radial plane fins (P5)	SS316L	68.0	6.0	5755	0.70	0.36
IWP lattice v2 (P3.v2)	SS316L	148.1	6.0	6620	0.54	0.41
Radial plane fins v2 (P5.v2)	SS316L	150.0	6.0	5214	0.54	0.41

numerical simulations of metal foam, graphite foam, and topologically optimized fins. Graphite foam presented the fastest PCM melting rate, while a multi-criteria decision-making evaluation identified the best-performing configuration to be 3% topologically optimized aluminium fins with 98% copper foam, based on energy storage time, density and overall efficiency. Guo et al. [23] tested a 3D-printed aluminium lattice thermal energy storage (TES) plate filled with N-tetradecane PCM in a vacuum chamber. The lattice structure demonstrated a 13-fold thermal conductivity increase compared to pure PCM, highlighting the potential of additively manufactured thermal conductivity enhancers for space applications.

For space applications, it is also crucial to understand the performance of PCM-based heat sinks under orbital conditions such as vacuum and microgravity. Simulating microgravity on Earth, however, is challenging due to high cost and limited test durations. Varying the orientation of the heat sink may provide a practical way to examine how gravity direction influences PCM melting and redistribution, and previous experimental studies for atmospheric pressure report that heat sink orientation has a minor role in thermal performance [24,25]. Studies of orientation effects under vacuum conditions have not been conducted to date.[1]

[1] Scopus search string: "TITLE-ABS-KEY(PCM AND orientation AND vacuum AND heat sink)"; Web of Science all fields search "PCM orientation vacuum heat sink" returned zero results on 12 Sep 2025

Table 1 summarizes the representative studies of finned or TPMS PCM-based heat sinks for spacecraft applications reviewed in this section. These examples illustrate the growing interest in PCM thermal storage for satellites and also the limited number of experimental investigations performed under vacuum or varied orientations conditions. For a comprehensive overview of PCM use in space systems, including applications in thermal management and beyond, readers are referred to the detailed review by Diaconu et al. [26].

While additively manufactured thermal conductivity enhancers have been widely explored for terrestrial applications, research on triply periodic minimal surface structures for satellite thermal management remains limited. As observed in Table 1, space-focused studies focus mostly on numerical simulations, with few experimental validations in vacuum environments. The present work addresses this gap through an experimental comparison of additively manufactured TPMS and finned PCM heat sinks for satellite thermal management. This study was carried out during the initial stages of the design development of Matilda, the University of Technology Sydney's payload for orbital experiments of satellite thermal management, launched to orbit in August of 2024 as part of the Waratah Seed-1 mission. To determine the most suitable heat sink geometry for inclusion in the payload, this work experimentally compares the thermal performance of three TPMS PCM-based heat sinks and a radial-finned heat sink, against a heat sink without thermal conductivity enhancers (TCE). The investigated internal designs were: no TCE/hollow (P1), gyroid-cells (P2), IWP lattice cells (P3), swirl lattice (P4), and radial plane fins (P5). The heat sinks were 3D-printed in titanium and stainless

Table 3
Material properties for tested components [28,29].

Material	Density (kg/m^3)	Thermal conductivity (W/mK)	Melting point (°C)	Specific heat capacity C_p (J/kgK)	Latent heat capacity H (J/kg)
Titanium Ti-6Al-4V	4850	11.4	–	544	–
Stainless steel SS316L	8000	16.2	–	500	–
Paraffin wax	880	0.2	53–58	2000	170 000

steel, and tested in a thermal vacuum chamber at two power input levels. Paraffin wax PCM was used. The influence of geometry and key parameters such as internal surface area and mass was assessed and discussed. To further examine the influence of gravity orientation on PCM melting and redistribution, the performance of PCM-based heat sinks is also assessed at different orientations under vacuum conditions, namely 0° (upright position), 90°, and 180° and varying initial PCM position within the heat sink. The novelty of this work lies in experimentally investigating multiple designs of TPMS PCM-based heat sinks for satellite thermal management and orientation effects under vacuum, two aspects underexplored in previous studies.

2. Methodology

2.1. Heat sink material and designs

Five different PCM-based heat sinks were designed and manufactured for assessing their thermal response in a vacuum environment. The heat sinks were identical in external size and shape, varying only in their internal structure geometry. Their external dimensions were 30 x 30 x 30 mm, their wall thickness was 1 mm, and they featured four lugs for mounting onto the electric heater and two PCM injection holes as shown in Figs. 1(a) and 1(b). The internal structures serve as thermal conductivity enhancers to the PCM, aiming to increase heat transfer from the heat source to the PCM. As shown in Fig. 1(c), the internal designs investigated in this work were: no TCE/hollow (P1), gyroid-cells (P2), IWP lattice cells (P3), swirl cells (P4), and radial plane fins (P5). The TPMS-based designs (P2-P4) had cells of 7 x 7 x 7 mm. The swirl lattice (P4), featuring curved cellular structures, follows the design introduced and numerically analysed by Arqam et al. [27]. The details of the five heat sink designs are summarized in Table 2, where $A_{structure}$ is the surface area of the internal TCE structure, $V_{void}/V_{overall}$ is the ratio between the internal void volume and the total overall volume. Given the complexity of some of these internal structures, the heat sinks were additively manufactured using laser powder bed fusion process (LPBF) in a GE Concept Laser M2 series 5 (400 W) machine in titanium Ti-6Al-4V and in stainless steel SS316L. While both materials are widely used in powder bed fusion manufacturing, they display distinct thermal and physical characteristics, allowing a comparative analysis. The materials properties are listed in Table 3. Titanium is characterized by a lower density and thermal conductivity compared to stainless steel, making it advantageous for weight sensitive applications, at the expense of heat conduction efficiency. Both titanium and stainless steel are suitable for thermal management solutions under harsh environments due to their high resistance to corrosion and effective shielding against radiation.

For further exploration of the internal surface area and mass effect on heat sink performance, an updated version of the IWP lattice P3 and radial-finned P5 heat sinks with matched masses was designed and manufactured for further testing, referred to as P3.v2 and P5.v2 in this work. Similarly to the original version, P3.v2 and P5.v2 heat sinks were manufactured via laser powder bed fusion, in stainless steel SS316L, and their details are listed in Table 2. The updated P3.v2 and P5.v2 heat sinks, displayed in Fig. 2, feature the mounting lugs near the bottom surface of the heat sink. In addition, they feature an increased wall thickness of 3 mm to mitigate possible leakage of liquid paraffin through microscopic voids in the structure, exacerbated in vacuum environments due to the absence of external pressure to counterbalance the internal pressure originated from the PCM's thermal expansion during melting. This design refinement was particularly relevant to increase the reliability of the University of Technology Sydney's Matilda payload. Cell size was reduced to 6 x 6 x 6 mm to accommodate the increased thickness.

The PCM used in the experiments was the Sigma-Aldrich 327204 paraffin wax, an organic solid–liquid PCM with melting point ranging from 53 to 58 °C, which was intentionally chosen to match the typical operating temperature window of satellite electronics. During flight, on-board electronics often operate between 20 °C and 85 °C, with failure typically occurring above the upper end of this range [30]. Using a phase change material with such melting temperature ensures that the latent heat storage process activates closer to the thermal limit of the electronics for both 50% and 100% duty cycle levels tested, both titanium and stainless steel heat sinks, across the five different internal designs. The chosen PCM therefore offers a good balance between relevance to satellite applications, energy storage capacity, and phase change duration for the heat sink materials and heat fluxes used in this work. A paraffin wax type was selected for its high energy storage capacity, uniform melting behaviour, and chemical and physical stability over repeated thermal cycles, which is paramount to satellite applications. The physical properties of this PCM are listed in Table 1. For a consistent comparison, all heat sinks were filled with 6.0 g of PCM, corresponding to approximately 50% of the internal void volume for the most geometrically constrained design (gyroid P2) when PCM was solid (contracted). This quantity was selected to ensure that no PCM overflow would occur during melting, as preliminary tests revealed that the PCM expansion during phase change is significantly more pronounced in vacuum conditions than at atmospheric pressure given the absence of external pressure to counteract volumetric expansion [18]. Preliminary incremental filling tests confirmed that 7.0 g caused leakage, whereas 6.0 g provided a safety margin to avoid overflow, maintain cleanliness inside the vacuum chamber, and ultimately minimize risk of leakage for the actual payload, as any minor leaks could damage nearby payloads and lead to mission failure. Although this amount represents less than the total cavity volume, it provides a consistent reference PCM mass across all designs, ensuring that the observed performance differences arise from geometry and material effects rather than PCM quantity.

2.2. Experimental setup

A known heat flux was applied at the base of each heat sink for a preset duration and observed its thermal response in a vacuum environment. The experimental setup is illustrated in Fig. 3. A 30 x 30 mm flat electric heater embedded on a printed circuit board (PCB) simulates the thermal dissipation of electronics by providing the desired heat flux. The PCB heater system, including thermal sensors, control electronics and software, was developed by the industry partner Mawson Rovers. The heater was regulated by a BeagleBone Black microcontroller, which also logged temperature measurements from thermistors and transmitted data wirelessly to a real-time online dashboard with cloud storage and remote control features. The PCB contained five thermistors soldered in the heater region to measure the base temperature of the

(a)

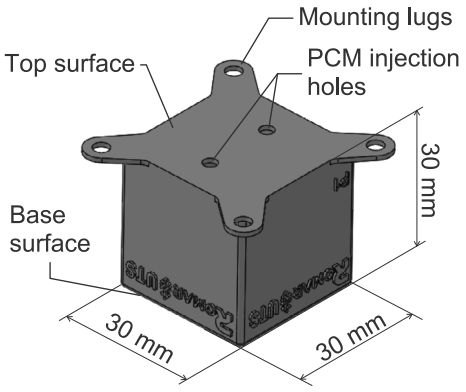

(b)

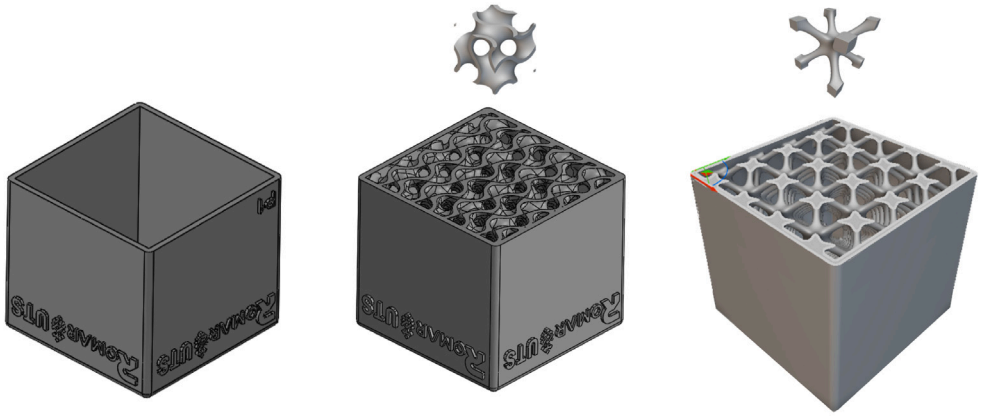

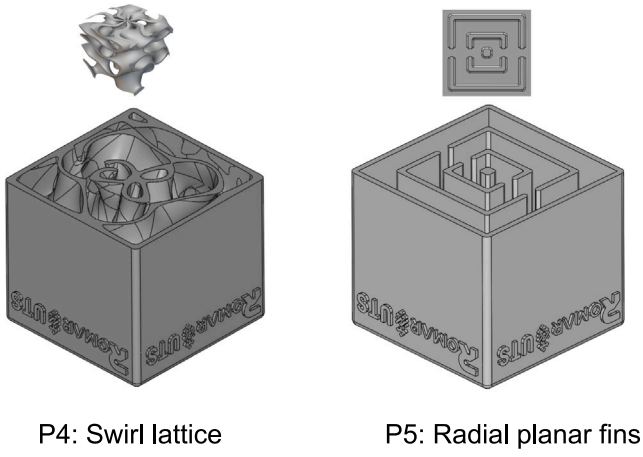

(c)

Fig. 1. Heat sinks used in this work for the comparison of multiple designs. (a) Example manufactured heat sink picture, (b) External dimensions, (c) Heat sink designs without top surface for visualization of the internal structure: No TCE/hollow (P1), Gyroid cells (P2), IWP lattice cells (P3), Swirl cells (P4), Radial planar fins (P5).

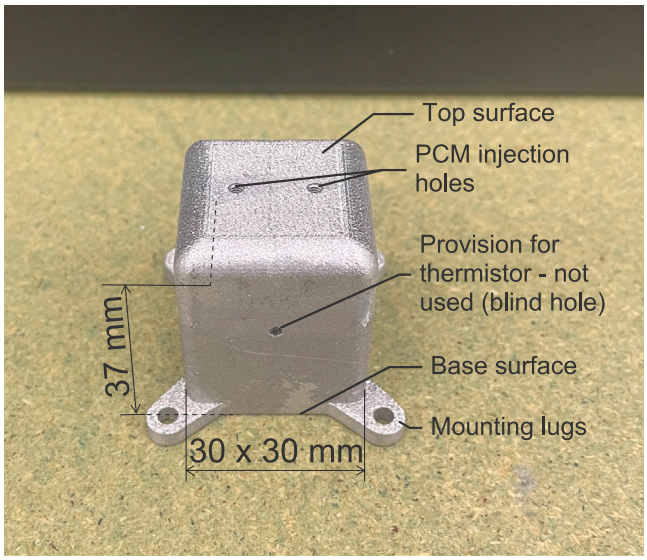

(a)

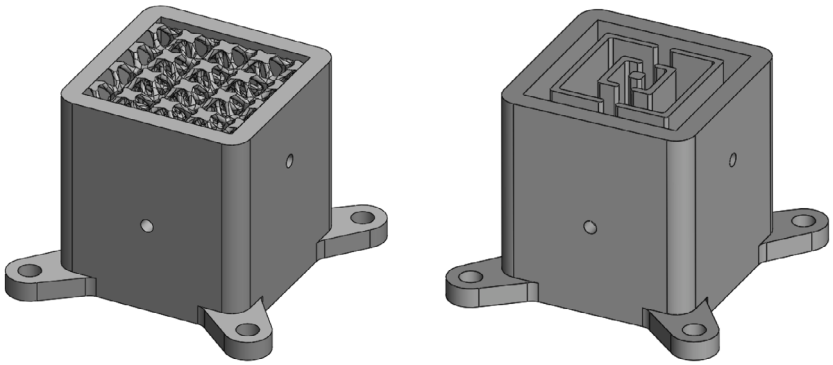

(b)

Fig. 2. Heat sinks used in this work for the mass-matched designs comparison and orientation study: (a) Example manufactured heat sink picture with external dimensions, (b) Heat sink designs without top surface for visualization of the internal structure: IWP lattice cells (P3.v2) and Radial planar fins (P5.v2).

heat sink, as well as an additional thermistor that was affixed to the top surface to monitor its temperature. The readings of the thermistor located at the centre of the heater are reported in this work, as they were typically the highest among the all heater thermistors and if they are too high would damage the electronics. They are referred in the results section of this work as T_{base}, or temperature at the base of the heat sink, while the readings from the free-hanging thermistor are referred as T_{top}. The temperature readings were recorded every 5 s.

A 5 V portable battery was used to power both the PCB and Beagle-Bone. Pulse width modulation (PWM) control was used to operate the heater, with experiments conducted at 100% and 50% duty cycles. A 100% duty cycle indicates the heater running continuously, while 50% duty cycle means the heater pulses between on and off states, delivering an average power equal to half of the 100% duty cycle condition. The power supplied by the heater P_{heater} was determined by Eq. (1) below with its voltage (U) and resistance (R). With a multimeter, voltage readings showed values of 4.8 V, while the resistance was determined as a function of the heater temperature, T, as given in Eq. (2). The power levels used in this study reflect typical operating scenarios of CubeSat electronics, which shift between operation (high power) and standby periods (low power) [3,31]. The uncertainty in power was calculated to ± 0.21 W from the independent variables voltage and resistance as demonstrated in Section 2.2.1. Authors' previous study [32] revealed that part of P_{heater} was lost through the mounting assembly, reducing the actual heat flux reaching the heat sink base to $P_{\text{heat sink}}$. The correction factors applies in Eqs. (3a) and (3b) were established from an earlier energy balance under comparable experimental conditions, including mounting assembly configuration and vacuum level [32].

$$P_{heater} = (duty\%)\frac{U^2}{R} \tag{1}$$

$$R = 0.0192T_{base} + 2.7774 \tag{2}$$

$$\frac{P_{\text{heat sink}}}{P_{\text{heater}}} = -0.008085(T_{\text{base}} - T_{\infty}) + 1.003416, \quad \text{50\% duty cycle} \tag{3a}$$

$$\frac{P_{\text{heat sink}}}{P_{\text{heater}}} = -0.004342(T_{\text{base}} - T_{\infty}) + 0.985953, \quad \text{100\% duty cycle} \tag{3b}$$

where T_{base} represents the electronics temperatures (coincident with the temperature at the base surface of the heat sink), and T_{∞} is the ambient temperature.

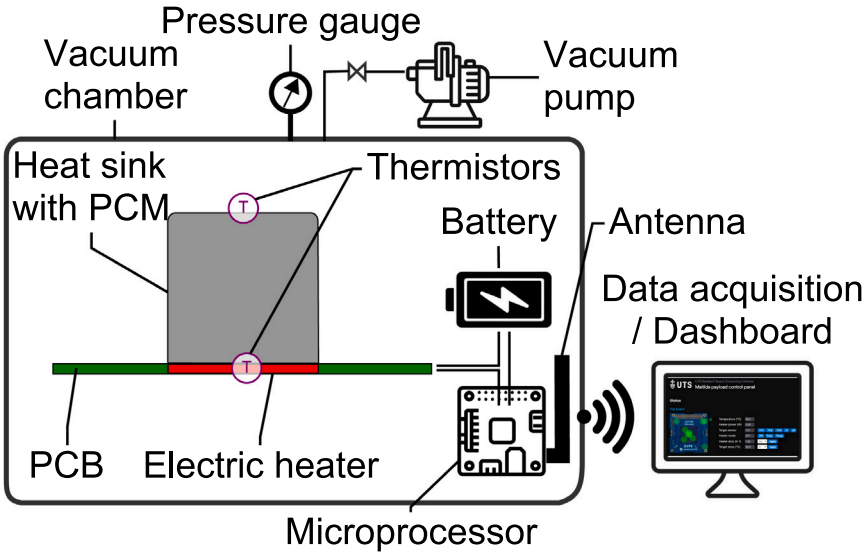

(a)

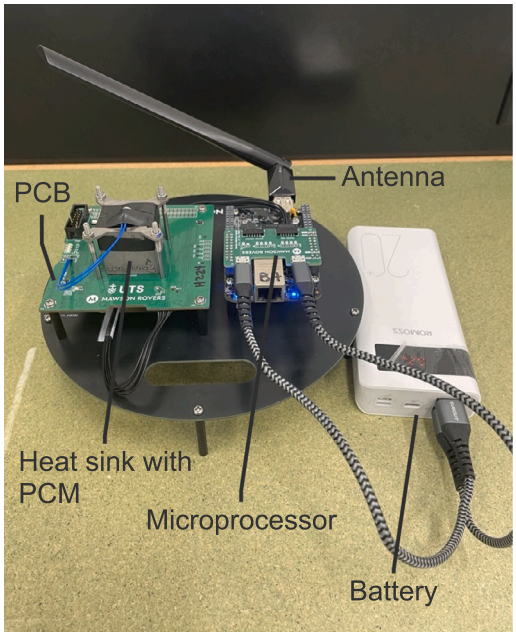

(b)

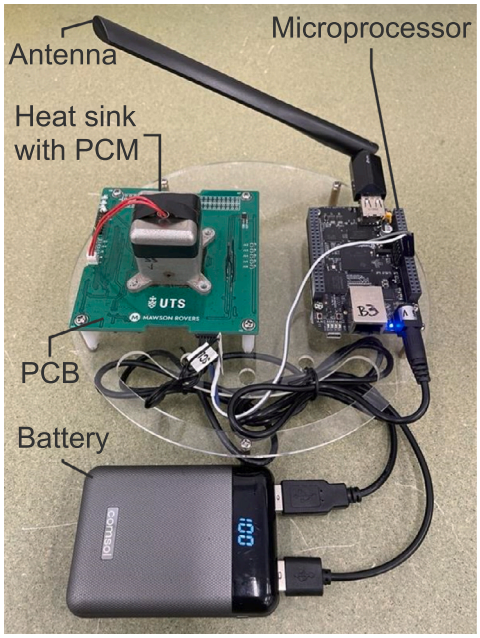

(c)

Fig. 3. Experimental setup: (a) Schematics, (b) Test rig picture for multiple designs comparison, (c) Test rig picture for mass-matched designs (P3.v2 and P5.v2) comparison and orientation study.

2.2.1. Uncertainty analysis

The uncertanties associated with the measured quantities are summarized in Table 4. The power uncertainty was calculated from Eq. (4), considering the worst-case scenario for independent quantities voltage and resistance: voltage of 4.8 V (highest) and resistance of 3.2 Ω (lowest, at 23 °C):

$$\delta_P = \sqrt{\left(\frac{\partial P}{\partial U}\cdot\sigma_U\right)^2 + \left(\frac{\partial P}{\partial R}\cdot\sigma_R\right)^2} = \sqrt{\left(\frac{2U}{R}\cdot\sigma_U\right)^2 + \left(-\frac{U^2}{R^2}\cdot\sigma_R\right)^2} \quad (4)$$

Table 4
Measurement uncertainties.

Parameter	Device	Uncertainty (%)	Uncertainty (σ)
Voltage	Multimeter	± 1.5%	± 0.07 V
Resistance	Multimeter	± 0.5%	± 0.02 Ω
Temperature	Thermistor	± 1.0%	± 0.25 °C
Power	Dependent variable	± 2.9%	± 0.21 W

2.3. Experimental test procedure

2.3.1. Effect of heat sink materials and designs on thermal performance

The pre-test procedure for the comparison across the five different heat sink designs, in both titanium and stainless steel material is as follows. 6.0 g of liquid paraffin wax was injected into each heat sink through the PCM injection holes with a syringe. During this step, the heat sink was maintained at a temperature above the PCM melting point to prevent unwanted premature PCM solidification and therefore uneven PCM distribution. The PCM injection holes were then sealed with pressure-rated gaskets and screws and the system was left to cooldown. Ambient temperature, maintained at 23 °C+/-1.5 °C

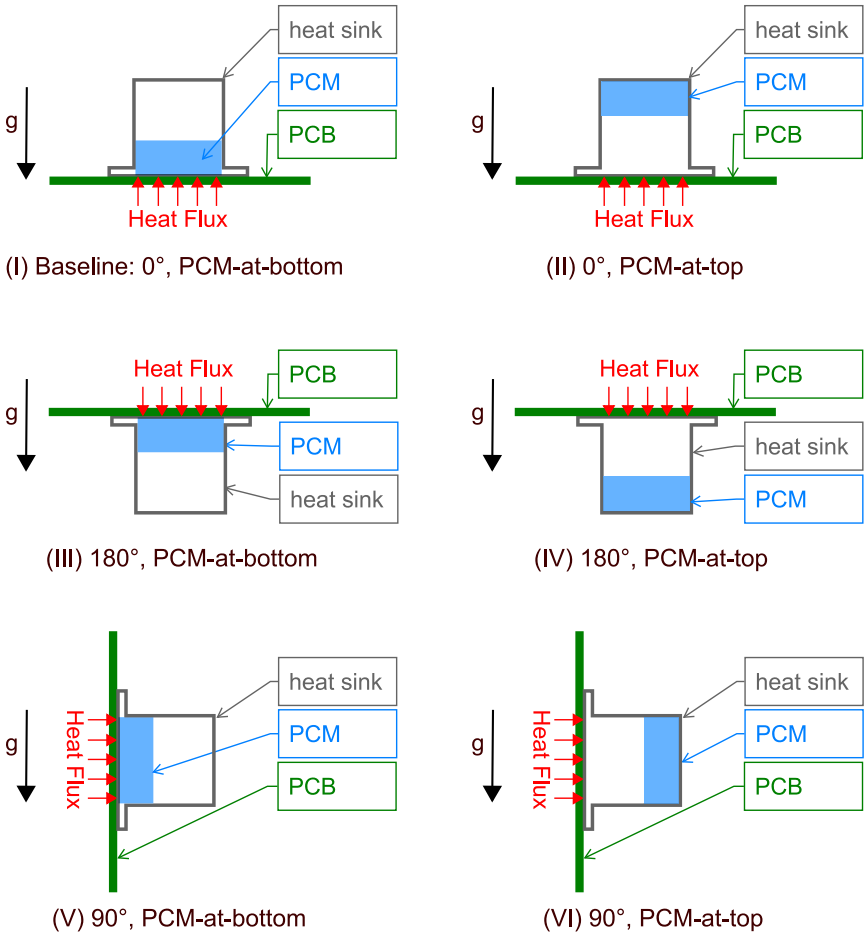

Fig. 4. Orientation and PCM initial position schematics for cases (I) to (VI) studied.

throughout the experiments. Each heat sink design and material combination was assembled on the heater with the PCM injection holes facing up. Testing was performed in isolation, that is, each heat sink was tested alone. The heat sink was attached to the PCB with bolts and nuts, as shown in Fig. 3(b), with a coat of Apiezon H thermal paste between heater and heat sink surfaces to ensure minimal contact resistance. The setup was placed inside a vacuum chamber, where the operating pressure was kept at 5 Pa. The heater was turned on at either 50% or 100% duty cycle and it remained running for 60 min or upon reaching a setpoint temperature of 100 °C. With the heater turned off, the system was left to cool for 60 min. Each test was conducted multiple times for reliable measurements, refer to the appendix for the experimental data range. All tests were performed under the same conditions (PCM quantity, thermal paste quantity, ambient temperature, and vacuum level), such that only the heat sink internal geometries varied between tests. A summary of the experiments performed to compare the heat sink materials and designs is listed in Table 5.

For the mass-matched designs comparison and orientation study, the mass-matched IWP lattice (P3.v2) and radial-finned (P5.v2) heat sinks underwent the same preparation, heating and cooling process as the original designs: each heat sink was filled with 6.0 g of paraffin wax, the heat sink was mounted onto the PCB heater, and placed inside the vacuum chamber. The key difference with these experiments was that the heat sinks were mounted onto the PCB with shorter screws, given the mounting lugs position, as shown in Fig. 3(c). Only the 100% duty power level was tested.

2.3.2. Effect of heat sink orientation and initial PCM position on thermal performance

Besides comparing the operation of different heat sink materials and designs under vacuum conditions, this study analysed the behaviour of PCM-based heat sinks at different orientations, to gain insights on how microgravity could potentially affect performance. To do so, distinct orientations were explored. These are 0° (upright position), 90°, and 180° (upside down), as shown in Fig. 4. In addition, the initial position of the PCM within the heat sink was also varied. Before testing, the PCM was pre-cooled to solidify either at the bottom of the heat sink or at the top, as illustrated in Fig. 4. A total of six cases were analysed: (I) baseline case, 0°, PCM-at-bottom; (II) 0°, PCM at top; (III) 180°, PCM-at-bottom; (IV) 180°, PCM-at-top; (V) 90°, PCM-at-bottom; and (VI) 90°, PCM-at-top. These tests, summarized in Table Table 6, were performed with the mass-matched version of the stainless steel IWP lattice P3.v2 and radial-finned P5.v2 heat sinks.

3. Results and discussion

The experiments with five different internal designs of titanium Ti-6Al-4V and stainless steel SS316L heat sinks under vacuum conditions yielded the results shown and discussed in the following sections. The internal designs studied in this work were hollow (P1), gyroid-cells (P2), IWP lattice cells (P3), swirl cells (P4), and radial plane fins (P5).

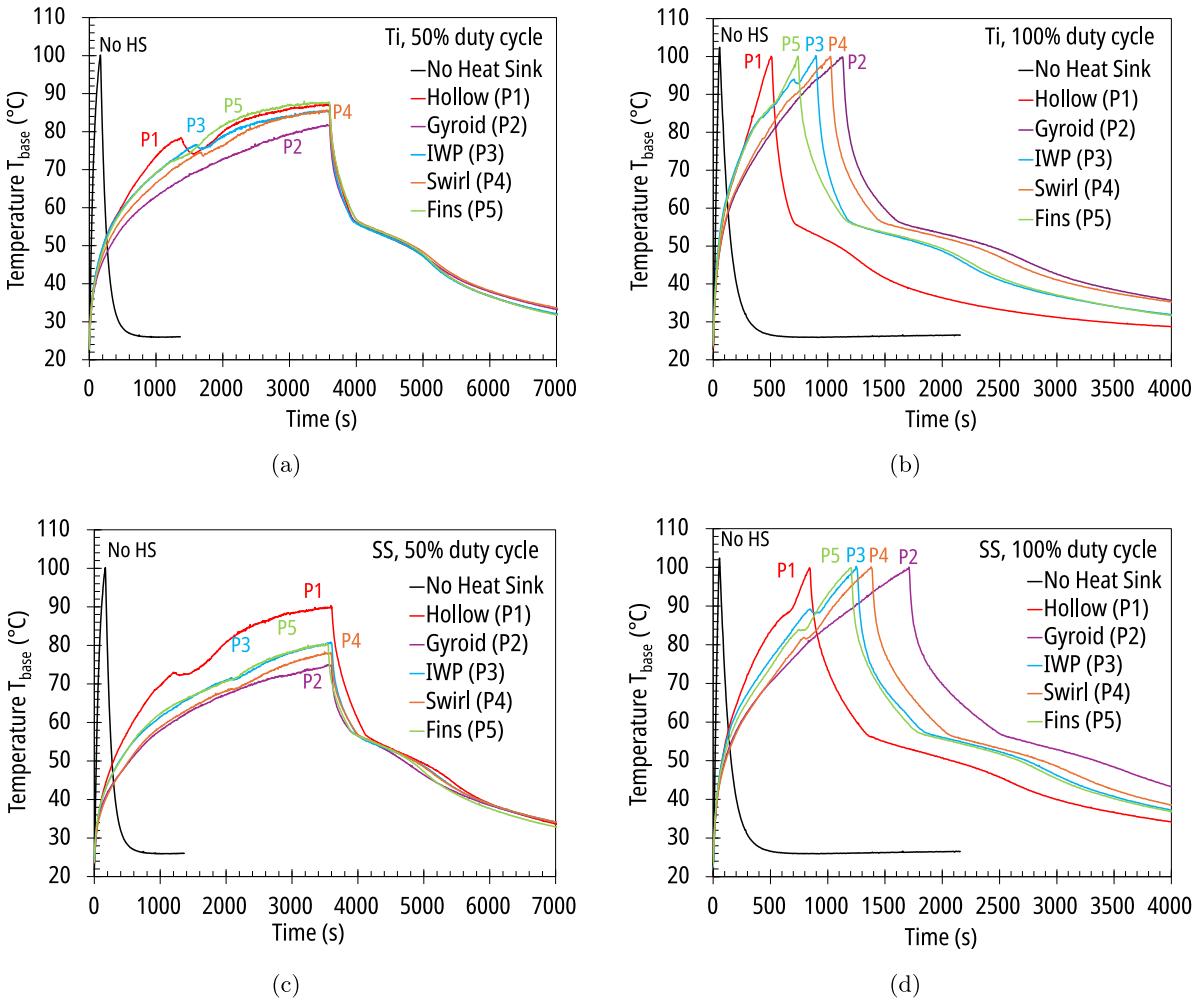

Fig. 5. Transient temperature results of experimental comparison across the five heat sink designs tested under vacuum conditions. (a) Titanium heat sinks at 50% duty cycle, (b) Titanium heat sinks at 100% duty cycle, (c) Stainless steel heat sinks at 50% duty cycle, (d) Stainless steel heat sinks at 100% duty cycle.

3.1. Comparison of heat sink materials

The experimental results indicate that titanium heat sinks exhibited higher temperatures than stainless steel heat sinks for both power levels, as shown in Fig. 5. Figs. 5(a) and 5(c) show that, at 50% duty cycle, the temperatures achieved at the end of the 60-minute heating phase ranged between 80 and 86 °C for titanium, whereas stainless steel heat sinks remained below 80 °C, except for the hollow design P1, which reached approximately 90 °C. Under 100% duty cycle, the titanium heat sinks achieved the setpoint temperature of 100 °C more rapidly than the stainless steel heat sinks, as shown in Figs. 5(b) and 5(d). This behaviour can be attributed to the lower thermal conductivity of Ti64, which is approximately 40% of SS316L. The reduced thermal conductivity restricts heat transfer from the base of the heat sink upwards, delaying heat absorption by the PCM. Similar results have been predicted in the authors' previous study [17], for PCM-based titanium and stainless steel heat sinks operating under atmospheric pressure. Understanding this behaviour of heat sinks with different materials is particularly relevant to systems operating in vacuum, where surface heat dissipation to the surroundings is relatively small, making thermal conduction the dominant mechanism for diverting heat away from the electronics.

PCM melting was observed for all designs of both titanium and stainless steel, under both heating power levels. Although melting was not obvious from the thermistor data during heating for the gyroid cells heat sink (P2), regardless of the material and heating power, it was visible during the cooling processes for this design. The high metal to PCM mass ratio likely masked the effect of the latent heat absorption during heating. The titanium hollow heat sink (P1) also showed no clear indication of PCM melting during heating at 100% duty cycle, likely due to its relatively low effective thermal conductivity, which limits efficient heat transfer to the PCM. As a result, localized PCM melting may occur near the base of the heat sink, creating an isolated region of liquid PCM rather than a well-distributed phase change, which hinders heat transfer due to PCM's low thermal conductivity. The ineffective heat transfer to the PCM can also explain the temperature drop observed during the melting phase of P1 design at 50% power level, as a solid mass PCM likely abruptly melted, absorbing latent heat, and leading to a sudden decrease in temperature at that instant.

3.2. Comparison of the different heat sink designs

In terms of the temperature curve profiles, the trend was similar for both materials under both power levels. Under 50% duty cycle (Figs. 5(a) and 5(c)), the gyroid-cells heat sink (P2) exhibited the lowest temperatures, whereas the hollow heat sink (P1) stood out as the highest-temperature case among the stainless steel designs. As the temperature profiles of the other designs exhibited overlapping and fluctuating trends, the average temperature during the 60-minute heating process was calculated for each design using Equation (5) [33]. Fig. 6 shows the ranking of average temperatures during the 60-minute heating for both materials. From lowest to highest, it begins with the

Table 5
Experimental tests conducted — Study of materials and designs. All heat sinks were filled with 6.0 g of PCM.

Test number	Heat sink details		Power level
	Design	Material	
1	No heat sink	N/A	50% duty
2	No heat sink		100% duty
3	Hollow (P1)	Ti-6Al-4V	50% duty
4	Gyroid (P2)		
5	IWP (P3)		
6	Swirl (P4)		
7	Radial fins (P5)		
8	Hollow (P1)		100% duty
9	Gyroid (P2)		
10	IWP (P3)		
11	Swirl (P4)		
12	Radial fins (P5)		
13	Hollow (P1)	SS316L	50% duty
14	Gyroid (P2)		
15	IWP (P3)		
16	Swirl (P4)		
17	Radial fins (P5)		
18	Hollow (P1)		100% duty
19	Gyroid (P2)		
20	IWP (P3)		
21	Swirl (P4)		
22	Radial fins (P5)		
23	IWP lattice v2 (P3.v2)		
24	Radial fins v2 (P5.v2)		

Table 6
Experimental tests conducted — Effect of orientation and initial PCM position. All tests used SS316L heat sinks with 6.0 g of PCM at 100% duty cycle.

Test number	Case	Heat sink design
25	(I): 0°, PCM-at-bottom	IWP lattice v2 (P3.v2)
26	(II): 0°, PCM-at-top	IWP lattice v2 (P3.v2)
27	(III): 180°, PCM-at-bottom	IWP lattice v2 (P3.v2)
28	(IV): 180°, PCM-at-top	IWP lattice v2 (P3.v2)
29	(V): 90°, PCM-at-bottom	IWP lattice v2 (P3.v2)
30	(VI): 90°, PCM-at-top	IWP lattice v2 (P3.v2)
31	(I): 0°, PCM-at-bottom	Radial fins v2 (P5.v2)
32	(II): 0°, PCM-at-top	Radial fins v2 (P5.v2)
33	(III): 180°, PCM-at-bottom	Radial fins v2 (P5.v2)
34	(IV): 180°, PCM-at-top	Radial fins v2 (P5.v2)
35	(V): 90°, PCM-at-bottom	Radial fins v2 (P5.v2)
36	(VI): 90°, PCM-at-top	Radial fins v2 (P5.v2)

gyroid-cells heat sink (P2), followed by the swirl cells heat sink (P4). Next is the IWP lattice heat sink (P3), followed very closely by the radial-finned design (P5), and, finally, the hollow heat sink (P1) with the highest average temperature. The case for the heater operating without a heat sink surpassed 100 °C in just 51 s. The similarity in the average temperature between stainless steel and titanium hollow design (P1) stems from the localized pool of molten PCM accumulated near the base of the heat sink given the lack of thermal conductivity enhancers, as explained in Section 3.1. Heat transfer from the base is then limited by the paraffin's low thermal conductivity rather than metal's property of the external walls. For P2 to P5 designs, however, the internal metallic structures (gyroid, IWP, swirl, and fins) provide more efficient paths for heat transfer within the PCM and the higher conductivity of stainless steel indeed enables faster heat distribution and PCM melting, resulting in lower overall base temperatures compared with titanium.

$$\overline{T} = \frac{1}{t_f - t_i} \int_{t_i}^{t_f} T(t)dt \tag{5}$$

For 100% duty cycle, a similar trend was observed in the operating time to reach the set point temperature of 100 °C, as shown in Figs. 5(b) and 5(d). The increase in operation time compared to the "No heat sink" case was computed and is presented in Fig. 7 for both titanium and stainless steel heat sinks. The gyroid-cells heat sink (P2) exhibited the most substantial increase in operating time among all the designs, followed by the swirl cells design (P4), the IWP lattice (P3) very close to the radial-finned design (P5), and the hollow design (P1) at last.

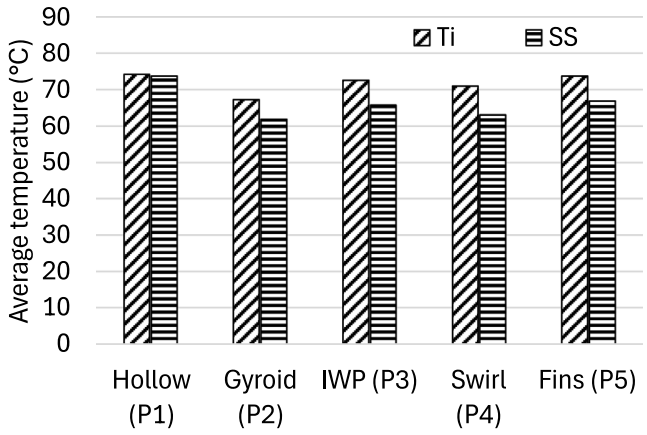

Fig. 6. Average temperature during the 60-minute heating for titanium and stainless steel heat sinks at 50% duty cycle.

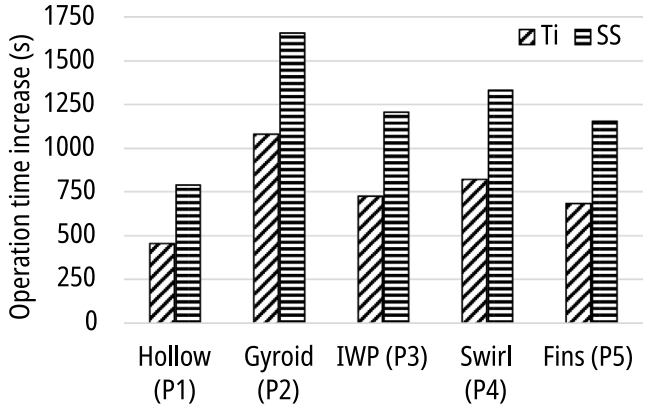

Fig. 7. Operation time increase to reach 100 °C for titanium and stainless steel heat sinks at 100% duty cycle, relative to test number 2, for the operation without a heat sink.

To understand the rationale behind these performances, the internal geometry areas and masses are compared in Fig. 8. Among all designs, the gyroid cells P2 possesses the largest internal surface area and is also the heaviest. For a comparative analysis across the designs, and to look at the effect of the internal surface area on the heat sink performance isolated, the IWP lattice (P3) and swirl cells design (P4) were examined in further detail as they possess nearly identical internal surface areas at just 1.5% difference. From Fig. 5(d), the stainless steel P3 and P4 increased the operating time by 1207 s and 1332 s relative to the "No heat sink" case. For titanium, these values were 725 s for P3 and 821 s for P4 (Fig. 5(b)). Therefore, despite this similarity in internal surface, P4 slightly outperformed P3 by operating around 10% longer for stainless steel, and approximately 13% longer for titanium. Since P4 is 17% heavier than P3 on both materials, it highlights the significant role of metal mass in heat sinks performance. A similar comparison was performed for the IWP lattice (P3) and the radial finned (P5) heat sinks, which have comparable masses. P3 is 8% heavier than P5 and features 20% more internal surface area. The performance of the heat sinks was

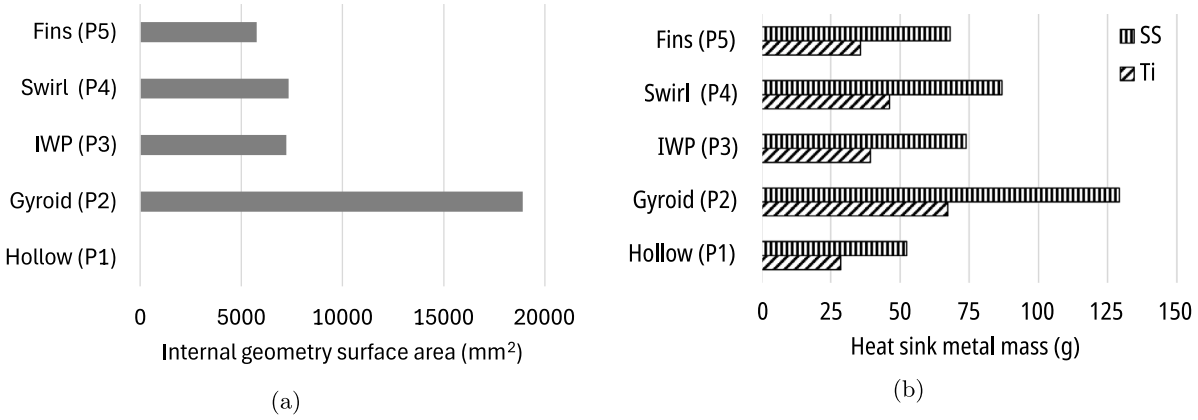

Fig. 8. Comparison of key parameters across the five heat sink designs tested under vacuum conditions. (a) Surface area of internal structure of heat sinks (mm^2) and (b) Metallic mass of heat sinks (g).

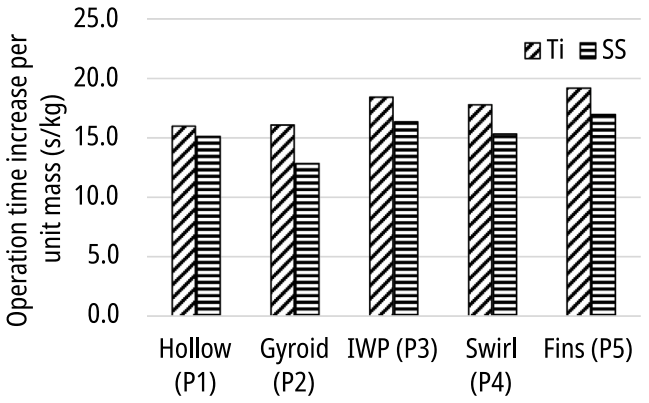

Fig. 9. Operation time increase per unit mass for titanium and stainless steel heat sinks at 100% duty cycle (s/kg).

close, with P3 increasing the operation time approximately 5% more than P5.

This analysis is particularly relevant to space applications, where minimizing payload mass is crucial due to high costs associated with satellite launches. To further quantify this aspect, the increase in operating time per unit mass was computed and displayed in Fig. 9. By this metric, the gyroid cells design P2 presented the lowest performance across the designs due to its substantially heavy structure. The radial finned heat sink (P5) demonstrated the highest "mass-benefit" ratio, followed very closely by the IWP lattice P3. Note that P3 and P5 designs differ in mass by only 8%.

3.2.1. Comparison of mass-matched heat sinks

To further investigate the effects of internal surface area and mass on heat sink performance, the mass-matched versions of the IWP lattice and radial-finned heat sinks, referred to as P3.v2 and P5.v2 respectively, were tested at 100% duty cycle. The mass difference between the updated heat sinks is minimal at 1.5%, while P3 features 27% more internal surface area than P5.

Fig. 10 exhibits the transient temperature profiles of the IWP lattice P3.v2 and the radial-finned P5.v2 designs. For context, it also includes the response of the original heat sink designs P3 and P5, which possess less metallic mass, as established in Table 2. In line with the observations of Section 3.2 regarding the relevance of overall mass, the updated designs P3.v2 and P5.v2 yielded overall lower temperatures and heating rates compared to their original designs with less mass.

The comparison between mass-matched IWP lattice P3.v2 and the radial-finned P5.v2 heat sinks in Fig. 10 reveals practically identical electronics temperatures (T_{base}) during heating, with a maximum difference of 2.5 °C at around 800 s, despite the 27% difference in internal surface area. The radial-finned design (P5.v2) exhibited slightly lower temperatures during the pre-melting sensible heating, despite the IWP lattice's increased surface area. This could be attributed to a greater mass concentration near the base of P5.v2 and, therefore, a more direct heat conduction path to the top surface of the heat sink, acting as a high-conductivity pathway for heat transfer. As a result, the top surface of P5.v2 is heated more rapidly than P3.v2, as observed in Fig. 10. In other words, the more direct heat conduction path in the radial-finned heat sink facilitates faster energy transfer throughout the structure and allows more rapid heat transfer to the solid PCM, leading to lower base temperatures during this phase. Conversely, the IWP lattice P3.v2 design features a more evenly distributed mass throughout the structure, resulting in a more dispersed heat transfer network. Although P3.v2's higher internal surface area should theoretically enhance heat transfer, its numerous interconnected walls may slow down heat conduction from the base, compared to the continuous and direct finned structure of P5.v2. This effect is evident by the lower temperatures observed at the top surface of P3.v2 heat sink compared to P5.v2, reinforcing the rationale that the finned geometry promotes a more direct heat conduction pathway.

After melting, the performance across both designs is nearly identical, with the IWP lattice heat sink (P3.v2) exhibiting slightly lower temperatures than the radial-finned heat sink (P5.v2). This could be attributed to enhanced buoyancy-driven convective heat transfer within the liquid PCM, facilitated by the more open porous structure of P3.v2. Unlike the more constrained flow path imposed by the radial plane fins, the porous nature of the IWP lattice may promote the formation of convection vortices within the molten PCM, as predicted for atmospheric pressure cases in the literature [34,35]. The similarity in performance between the mass-matched IWP lattice and finned heat sinks is in line with the numerical results reported by Arqam et al. [17] for the heating phase of heat sinks under atmospheric pressure. As suggested in Section 4, a detailed numerical simulation to visualize buoyancy-driven convection within the PCM for both cases would be a beneficial future research. The cooling rates are closely matched in the present study for both designs, with P3.v2 heat sink cooling slightly faster than P5.v2. This finding aligns with the results reported by Gopalan et al. [16] for

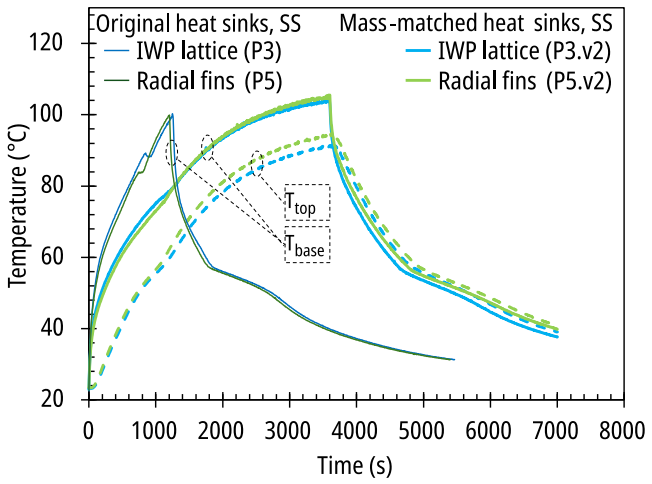

Fig. 10. Transient temperature results of the experimental assessment between the mass-matched version of IWP lattice (P3.v2) and radial-finned (P5.v2) stainless steel heat sinks at 100% duty cycle. The temperatures shown were recorded at the base and top surfaces of the heat sink, T_{base} and T_{top}, respectively.

PCM-based heat sinks under atmospheric pressure, where the type of internal geometry has a limited impact on the cooling behaviour.

This similarity in performance despite a 27% difference in surface area can be explained by considering the energy balance in the heat sink across the heating process:

$$P_{\text{heat sink}} = \Delta\dot{Q}_{stored} + q_{out} \tag{6}$$

$$\Delta\dot{Q}_{stored} = \Delta\dot{Q}_{stored,HS} + \Delta\dot{Q}_{stored,PCM} \tag{7a}$$

$$\Delta\dot{Q}_{stored} = \frac{m_{HS}C_{p_{HS}}(T_{HS,f} - T_{HS,i}) + m_{PCM}C_{p_{PCM}}(T_{PCM,f} - T_{PCM,i}) + \lambda m_{PCM}H_{PCM}}{t} \tag{7b}$$

$$q_{out} = \epsilon\sigma A_{external}(T^4_{surface} - T^4_{\infty}) \tag{8}$$

where $P_{\text{heat sink}}$ is the energy input from the heat flux applied at the base during the heating period (defined in Section 2), $\Delta\dot{Q}_{stored}$ represents the thermal energy stored in the system (both in the heat sink and the PCM), and q_{out} accounts for the energy dissipation from the external surface of the heat sink into the environment. Since both designs have the same mass, PCM content, external surface area $A_{external}$, and emissivity ϵ, their overall energy balance is sensitive to heat sink mass rather than differences in internal structures. The slightly different temperature evolution can be attributed to variations in localized heat transfer rates rather than differences in global energy balance.

Before melting, the heat transfer from the metal to the solid PCM is primarily governed by conduction as per Equation (9), where L_1 represents the conduction path length. Although the IWP lattice P3.v2 design has a larger $A_{structure}$, its lower metal temperatures result in a lower driving temperature difference $(T_{HS} - T_{PCM})$ compared to the radial-finned design P5.v5. Consequently, the rate of heat transfer to the PCM is higher than P5.v2, leading to lower base temperatures at the pre-melting stage.

$$q_{conduction} = \frac{k_{PCM}A_{structure}(T_{HS} - T_{PCM})}{L1} \tag{9}$$

After melting, the heat transfer from the metallic heat sink to the PCM transitions to a convective regime as shown in Eq. (10), where h is the convective heat transfer coefficient within the molten PCM. As the porous structure of P3.v2 may enhance buoyancy-driven convective vortices, a higher effective h is achieved, leading to faster heat transfer from metal to the liquid PCM and, consequently, to P3.v2's slightly lower base temperatures in the post-melting phase.

$$q_{convection} = h_{PCM}A_{structure}(T_{HS} - T_{PCM}) \tag{10}$$

Despite these localized differences in heat transfer rate, the total energy balance remains the dominant factor in determining the final steady-state temperature. Since both heat sinks have the same total mass and PCM content, they ultimately reach nearly identical thermal responses. This suggests that, under vacuum conditions where radiative losses dominate, the effect of internal geometry on overall performance could be secondary to the total thermal mass. Additional study of multiple heat sink designs with varying mass, internal surface areas, and external geometry would further isolate the independent effects of these parameters on thermal performance. It should be noted that this paper focused on a paraffin wax PCM with relatively low thermal conductivity and moderate viscosity, which could significantly influence heat transfer and melting dynamics. Variations may occur with different PCM types with varying properties, which could alter the relative influence of geometry and mass. Nevertheless, the trends observed in this work provide a strong reference for PCM classes with similar thermo-physical properties.

3.3. Effect of the heat sink orientation and PCM initial position on thermal performance

In addition to evaluating different heat sink materials and designs under vacuum conditions, this work examined the impact of heat sink orientation on thermal performance. Experiments were conducted at three orientations: 0° (upright), 90°, and 180° (inverted). Furthermore, the effect of the initial position of PCM within the heat sink was also analysed. The position was controlled by pre-cooling the PCM to solidify it either at the bottom or the top of the heat sink before testing. This setup resulted in six distinct test cases: (I) reference case—0° with PCM at the bottom; (II) 0° with PCM at the top; (III) 180° with PCM at the bottom; (IV) 180° with PCM at the top; (V) 90° with PCM at the bottom; and (VI) 90° with PCM at the top, as shown in Figure Fig. 4. Under vacuum conditions, a heat flux corresponding to 100% duty cycle was applied at the base of the heat sinks IWP lattice P3.v2 and radial-finned P5.v2 for 60 min, followed by a 60-minute cooldown period.

The temperature profiles resulting from these experiments are displayed in Figs. 11(a) and 11(b) for the IWP lattice P3 and radial-finned P5 designs, respectively. The temperature profiles were similar across all cases, indicating that neither orientation of the heat sink, nor the initial PCM position have a large impact on performance. The maximum temperature difference between the cases was 4.0 °C at approximately 730 s, during the PCM melting phase. At the end of the heating phase (3600 s), the maximum difference is 3.4 °C, while at the end of cooling (7200 s), the maximum difference is 2.4 °C.

Fig. 12 presents the transient base temperature difference for each case relative to the baseline case (I) (0°, PCM-at-bottom). Fig. 12(a) corresponds to the IWP heat sink P3, and Fig. 12(b) represents the finned heat sink P5. Both figures exhibit a consistent trend across the cases, with temperature differences following similar patterns for each phase of the heating–cooling process. During the pre-melting sensible heating phase, the temperature profile is impacted by the initial position of the PCM. For both the IWP P3 and finned P5 heat sinks, the PCM-at-bottom cases (III) and (V) displayed temperatures close to the baseline case (0°, PCM at bottom), varying from around −1.2 to around 0 °C. On the other hand, the PCM-at-top cases (II), (IV), and (VI) exhibited temperatures 2-4 °C higher than the baseline case (I). In these cases, the heat flux, applied at the base opposite to the PCM's initial location, took longer to reach the PCM. As a result, sensible heat absorption by the PCM was delayed, leading to higher temperatures. This also explains why the melting phase lasted longer for the PCM-at-top cases (II), (IV), and (VI), as observed in Fig. 11(a) and 11(b).

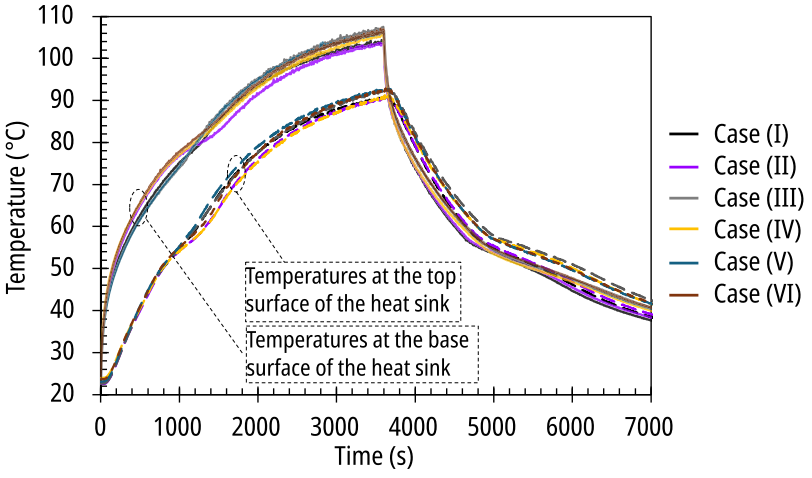

(a)

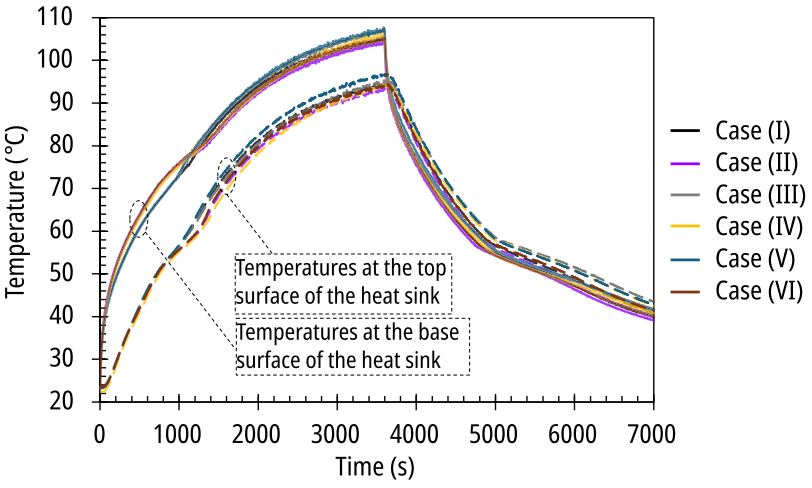

(b)

Fig. 11. Transient temperature results of the experimental assessment of orientation and initial PCM position for the mass-matched IWP lattice P3.v2 and radial fins P5.v2 designs. Cases: (I) 0°, PCM-at-bottom; (II) 0°, PCM at top; (III) 180°, PCM-at-bottom; (IV) 180°, PCM-at-top; (V) 90°, PCM-at-bottom; and (VI) 90°, PCM-at-top. See Fig. 4 for case arrangements. The temperatures shown were recorded at the base and top surfaces of the heat sink, T_{base} and T_{top}, at 100% duty cycle. (a) IWP lattice design P3.v2, (b) Radial fins design P5.v2.

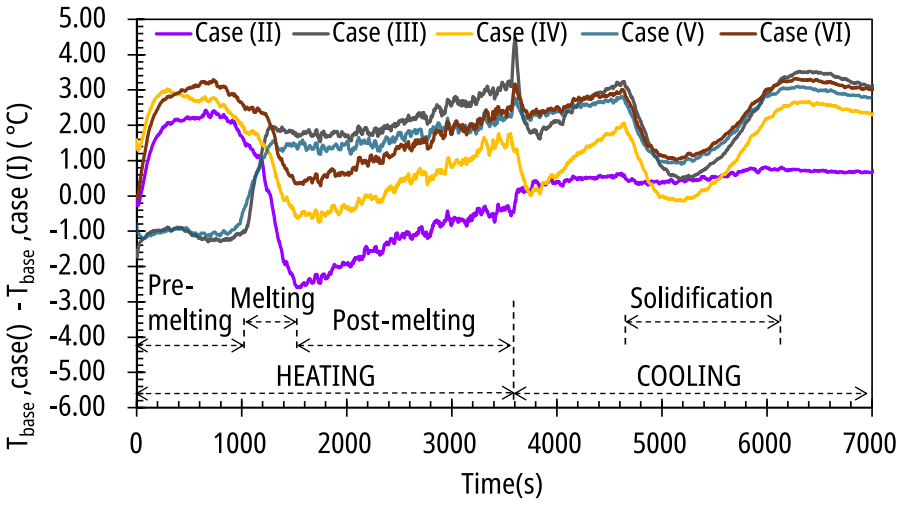

(a)

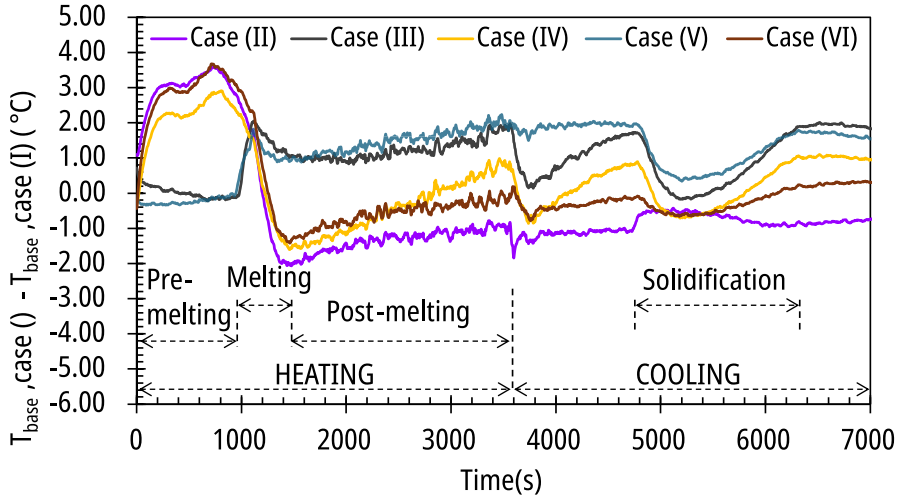

(b)

Fig. 12. Transient base temperature difference relative to the baseline case (I) for the orientation cases (II) to (VI) of the mass matched IWP lattice P3.v2 and radial fins P5.v2 designs. Cases: (I) 0°, PCM-at-bottom; (II) 0°, PCM at top; (III) 180°, PCM-at-bottom; (IV) 180°, PCM-at-top; (V) 90°, PCM-at-bottom; and (VI) 90°, PCM-at-top. See Fig. 4 for case arrangements. (a) IWP lattice design P3.v2, (b) Radial fins design P5.v2.

Interestingly, during the melting phase, there is a clear shift in the temperature difference relative to the baseline case (I), as observed in Fig. 12. Cases (III) (90°, PCM-at-bottom) and (V) (180°, PCM-at-bottom) begin to show a positive temperature difference relative to the baseline case, possibly because the liquid PCM is now far from the base, where heat flux is applied. As a result, the sensible heat absorption by the liquid PCM is comparably reduced, given that the top sections of the heat sink sustain lower temperatures than the base. Conversely, the PCM-at-top cases (II), (IV) and (VI) shifted to negative temperature differences relative to the baseline case (I). This effect occurs because PCM melting takes longer for these cases. Since PCM melts at a near-constant temperature, these cases displayed lower temperatures relative to case (I). For example, at 1000 s, melting in the baseline case is already complete, and the liquid PCM is absorbing sensible heat, whereas the PCM-at-top cases are still undergoing melting, resulting in lower temperatures for these cases. Once melted, the PCM settles in the same final position for each heat sink orientation, regardless of its initial placement. However, the PCM-at-bottom cases (I), (III) and (V) still sustain slightly higher temperatures compared to the PCM-at-top cases (II), (IV) and (VI) throughout the remainder of heating phase and cooling, especially for the radial-finned P5 design. A detailed CFD simulation would be necessary to fully understand the interplay between the heat sinks internal structure, PCM viscosity, thermal expansion, and buoyancy of the trapped air inside the heat sink. During the solidification process, the temperature difference across all cases converge to a minimal value, suggesting that the heat sink orientation does not have a significant impact in the release rate of stored latent heat. This study of the orientation of the heat sink and initial position of PCM demonstrated that, while the orientation has minimal impact on the thermal performance of the heat sink, the PCM position has a slightly higher influence, especially during the pre-melting sensible heating phase.

The key difference between the IWP (P3.v2) and radial-finned (P5.v2) designs in terms of orientation performance is that the IWP heat sink (P3.v2) exhibits a weaker orientation dependence, giving its more uniform temperature difference across the different orientations during post-melting sensible heating phase when the PCM is liquid. This reduced sensitivity to orientation and initial PCM position suggests that P3.v2's orientation-symmetric internal geometry promotes heat distribution more evenly regardless of the orientation, which could be a significant advantage for PCM-based systems in microgravity.

4. Conclusion

The results of this study demonstrated the thermal performance of TPMS and finned PCM-based heat sinks under vacuum conditions, focusing on heat sink design, material, and orientation. Titanium and stainless steel were compared across five designs: hollow, gyroid cells, IWP lattice cells, swirl cells, and radial fins. The results provide insights into the thermal behaviour of this type of passive thermal management systems for satellite applications.

Titanium heat sinks exhibited higher temperatures due to their lower thermal conductivity relative to stainless steel. In terms of heat sink designs, internal geometry significantly influenced performance: gyroid-cells heat sink exhibited the lowest temperatures, followed by swirl cells, then IWP lattice and radial fins with similar behaviour, and finally the hollow design, which achieved the highest temperatures. To identify factors influencing performance, the internal surface area and mass of each design was compared. This revealed the IWP lattice and radial finned designs as the most mass-effective. A subsequent study with a mass-matched version of these two designs revealed that, despite the IWP lattice featuring 27% more internal surface area than the radial-finned heat sink, both exhibited nearly identical thermal performances. This challenges the conventional assumption that increased surface area inherently improves heat transfer, and instead emphasizes the critical role of mass distribution within the heat sink layout.

Heat sink orientation and PCM initial position had only a minor impact on overall thermal performance. The temperature profiles remained similar across all tested orientations (0°, 90°, and 180°), with a maximum temperature difference of 4.0 °C during the PCM melting phase. PCM initially at the top delayed absorption slightly, but overall effects remained small. The IWP lattice heat sink exhibited slightly weaker dependence on orientation compared to the radial-finned design, reinforcing the suitability of TPMS structures for space applications, where microgravity and variable orientations are common.

Overall, these findings suggest that while material properties and total mass have a significant influence on PCM-based heat sink performance, orientation and initial PCM positioning have a relatively minor effect. The results emphasize that, for mass-limited applications such as spacecrafts, optimizing the distribution of metallic mass within the heat sink and material selection might yield greater benefits than merely maximizing surface area. In other words, strategic mass distribution and efficient thermal pathways can be more critical design drivers than geometric complexity for increased surface area alone.

Future work should focus on detailed numerical simulation to better visualize how the relation between the heat sinks internal structure, PCM viscosity, thermal expansion, and trapped air affect the heat transfer within the heat sink. Additionally, the influence of printing direction of the additively manufactured heat sinks and resulting uneven thermal contact between the PCM and the metallic walls should be investigated, as they could subtly affect melting uniformity and overall performance. Conducting further experiments at different power levels and PCM quantity, and/or other heat sink geometries and PCM properties would also benefit the analysis. Testing under real microgravity conditions is also critical to validate the performance of TPMS-PCM systems for spacecraft electronics cooling. This study was part of the design development of Matilda, the University of Technology Sydney's CubeSat thermal management technology demonstrator. The findings guided the selection of the most suitable heat sink design for inclusion in the payload, which was launched to orbit in August 2024 as part of the Waratah Seed-1 mission. The next stage of this research involves analysing in-orbit thermal performance data, which will provide valuable insight into the behaviour of PCM-based heat sinks in actual space conditions.

CRediT authorship contribution statement

Laryssa Sueza Raffa: Writing – original draft, Visualization, Methodology, Investigation, Formal analysis, Data curation, Conceptualization. **Matt Ryall:** Software, Resources. **Nick S. Bennett:** Writing – review & editing, Supervision, Resources, Funding acquisition. **Lee Clemon:** Writing – review & editing, Supervision.

Declaration of competing interest

The authors declare the following financial interests/personal relationships which may be considered as potential competing interests: Laryssa Sueza Raffa reports financial support was provided by the University of Technology Sydney and the Australian Government. Nick S. Bennett reports financial support was provided by SmartSat Cooperative Research Centre. If there are other authors, they declare that they have no known competing financial interests or personal relationships that could have appeared to influence the work reported in this paper.

Acknowledgements

This research was funded by the University of Technology Sydney, Australia, SmartSat Cooperative Research Centre, and the Australian Government Research Training Program.

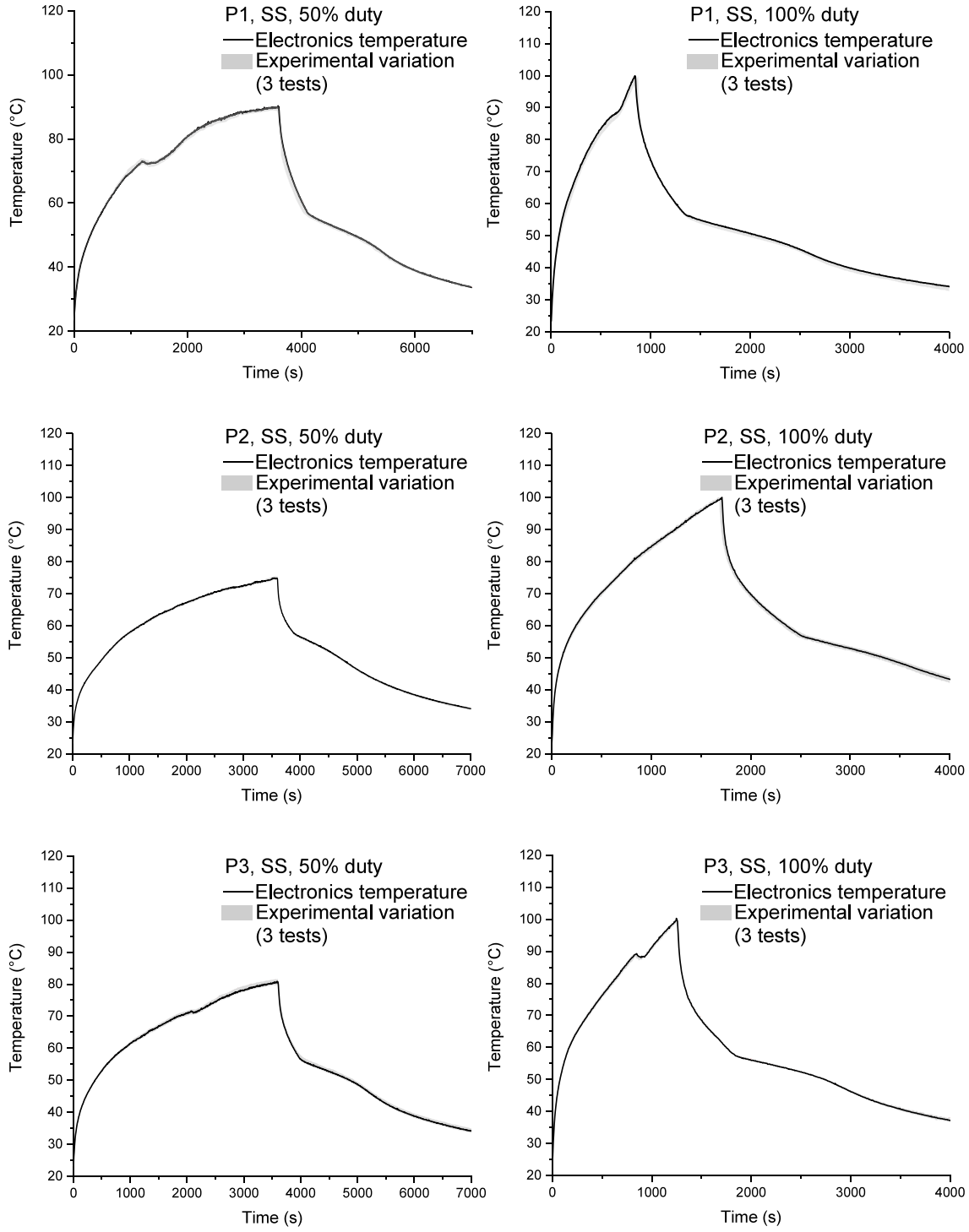

Fig. A.1. Appendix: experimental data range of multiple tests performed for each design/material/power case.

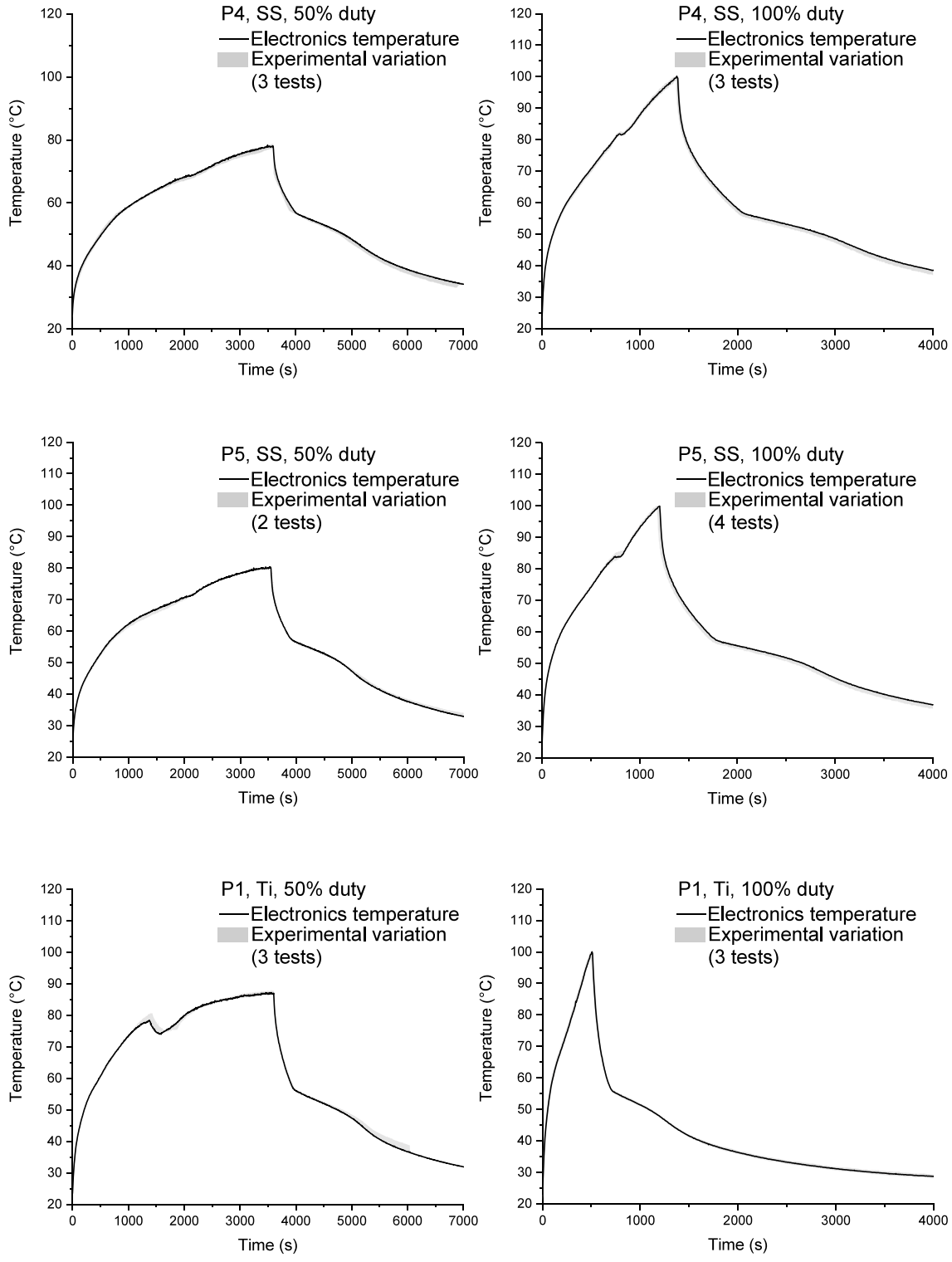

Fig. A.2. Appendix: experimental data range of multiple tests performed for each design/material/power case.

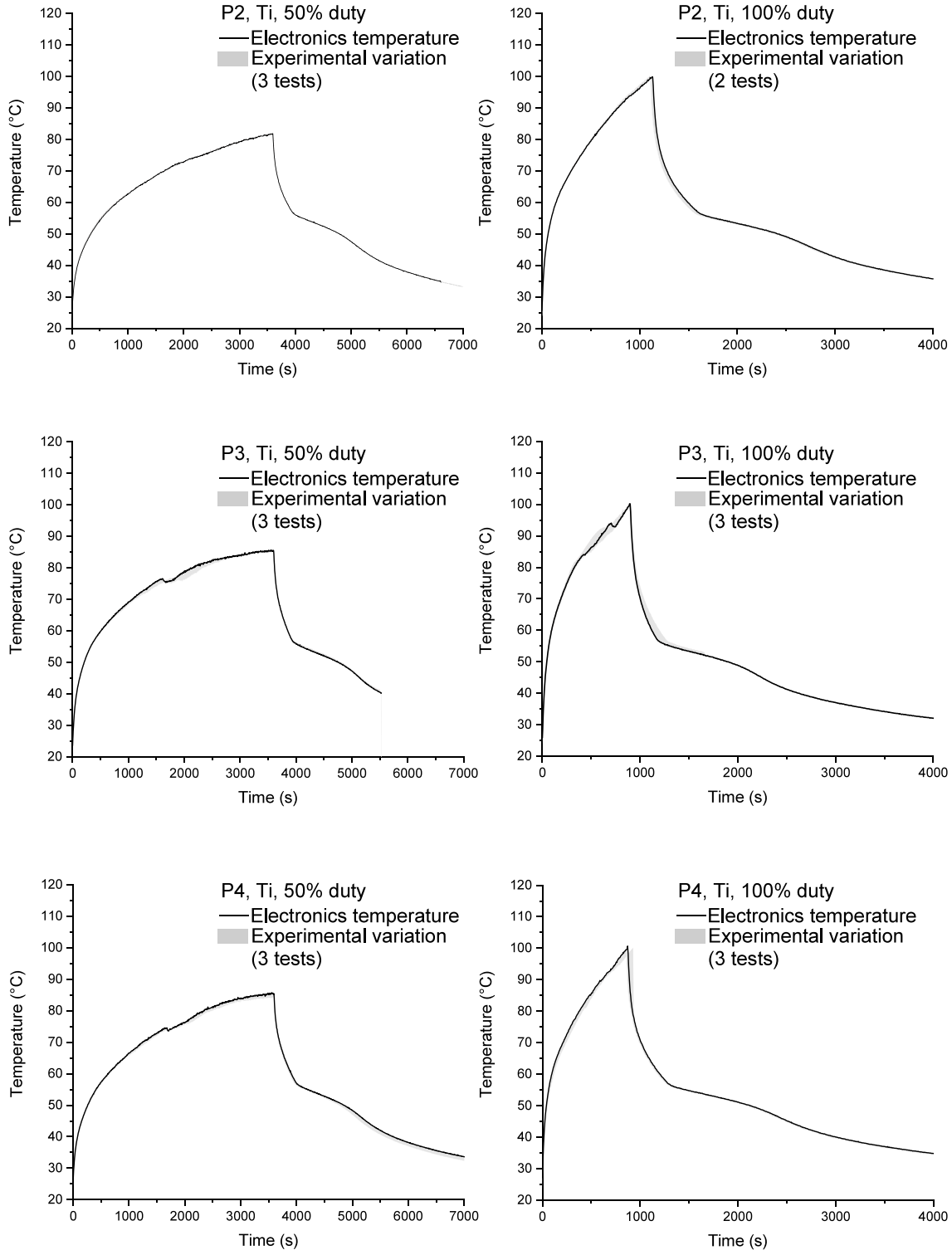

Fig. A.3. Appendix: experimental data range of multiple tests performed for each design/material/power case.

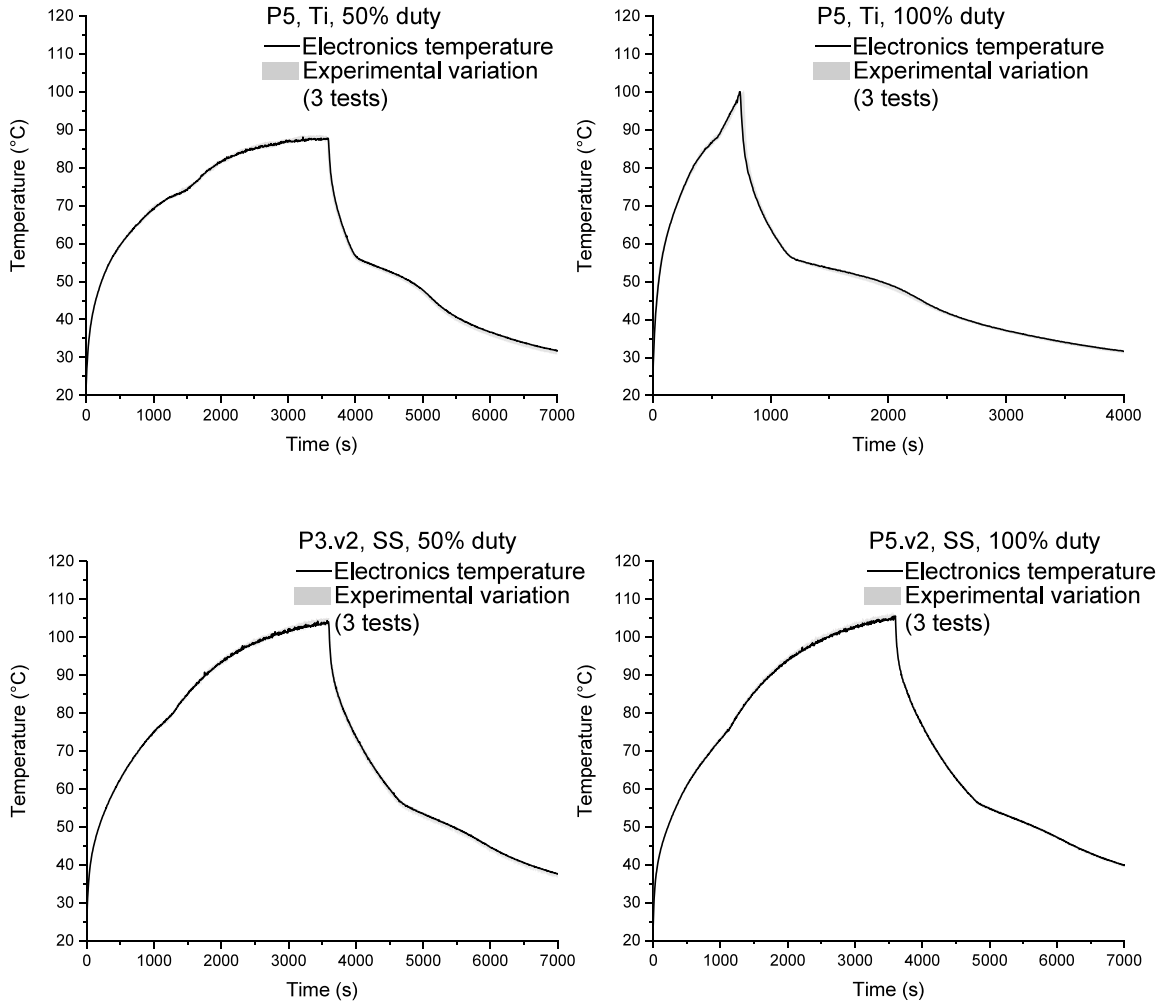

Fig. A.4. Appendix: experimental data range of multiple tests performed for each design/material/power case.

Appendix. Experimental data range

See Figs. A.1–A.4.

Data availability

Data will be made available on request.

References

[1] M. Pedram, S. Nazarian, Thermal modeling, analysis, and management in VLSI circuits: Principles and methods, Proc. IEEE 94 (8) (2006) 1487–1501, http://dx.doi.org/10.1109/JPROC.2006.879797, URL http://ieeexplore.ieee.org/document/1705138/.

[2] Y.A. Çengel, Heat and Mass Transfer: A Practical Approach, third ed., in: McGraw-Hill Series in Mechanical Engineering, McGraw-Hill, Boston, 2007.

[3] S.-J. Kang, H.-U. Oh, On-orbit thermal design and validation of 1 U standardized CubeSat of STEP cube lab, Int. J. Aerosp. Eng. 2016 (2016) 1–17, http://dx.doi.org/10.1155/2016/4213189, URL http://www.hindawi.com/journals/ijae/2016/4213189/.

[4] Y. Lin, Y. Jia, G. Alva, G. Fang, Review on thermal conductivity enhancement, thermal properties and applications of phase change materials in thermal energy storage, Renew. Sustain. Energy Rev. 82 (2018) 2730–2742, http://dx.doi.org/10.1016/j.rser.2017.10.002, URL https://linkinghub.elsevier.com/retrieve/pii/S1364032117313746.

[5] A.M. Elshaer, A. Soliman, M. Kassab, S. Mori, A. Hawwash, Experimental investigations on copper foam/PCM composite-based thermal control hardware (TCH) using foam samples with different pore sizes under intermittent thermal conditions, J. Energy Storage 72 (2023) 108320, http://dx.doi.org/10.1016/j.est.2023.108320, URL https://linkinghub.elsevier.com/retrieve/pii/S2352152X23017176.

[6] B. Xie, W.-l. Cheng, Z.-m. Xu, Studies on the effect of shape-stabilized PCM filled aluminum honeycomb composite material on thermal control, Int. J. Heat Mass Transfer 91 (2015) 135–143, http://dx.doi.org/10.1016/j.ijheatmasstransfer.2015.07.108, URL https://linkinghub.elsevier.com/retrieve/pii/S0017931015008261.

[7] N.I. Ibrahim, F.A. Al-Sulaiman, S. Rahman, B.S. Yilbas, A.Z. Sahin, Heat transfer enhancement of phase change materials for thermal energy storage applications: A critical review, Renew. Sustain. Energy Rev. 74 (2017) 26–50, http://dx.doi.org/10.1016/j.rser.2017.01.169, URL https://linkinghub.elsevier.com/retrieve/pii/S1364032117301739.

[8] Z. Maqbool, M. Hanief, M. Parveez, Review on performance enhancement of phase change material based heat sinks in conjugation with thermal conductivity enhancers for electronic cooling, J. Energy Storage 60 (2023) 106591, http://dx.doi.org/10.1016/j.est.2022.106591, URL https://linkinghub.elsevier.com/retrieve/pii/S2352152X22025804.

[9] P. Bose, V.A. Amirtham, A review on thermal conductivity enhancement of paraffinwax as latent heat energy storage material, Renew. Sustain. Energy Rev. 65 (2016) 81–100, http://dx.doi.org/10.1016/j.rser.2016.06.071, URL https://linkinghub.elsevier.com/retrieve/pii/S1364032116303033.

[10] R. Baby, C. Balaji, Experimental investigations on phase change material based finned heat sinks for electronic equipment cooling, Int. J. Heat Mass Transfer 55 (5–6) (2012) 1642–1649, http://dx.doi.org/10.1016/j.ijheatmasstransfer.2011.11.020, URL https://linkinghub.elsevier.com/retrieve/pii/S0017931011006570.

[11] A.N. Desai, A. Gunjal, V. Singh, Numerical investigations of fin efficacy for phase change material (PCM) based thermal control module, Int. J. Heat Mass Transfer 147 (2020) 118855, http://dx.doi.org/10.1016/j.ijheatmasstransfer.2019.118855, URL https://linkinghub.elsevier.com/retrieve/pii/S0017931019316655.

[12] S. Hosseinizadeh, F. Tan, S. Moosania, Experimental and numerical studies on performance of PCM-based heat sink with different configurations of internal fins, Appl. Therm. Eng. 31 (17–18) (2011) 3827–3838, http://dx.doi.org/10.1016/j.applthermaleng.2011.07.031, URL https://linkinghub.elsevier.com/retrieve/pii/S1359431111003905.

[13] S. Zhang, S. Mancin, L. Pu, A review and prospective of fin design to improve heat transfer performance of latent thermal energy storage, J. Energy Storage 62 (2023) 106825, http://dx.doi.org/10.1016/j.est.2023.106825, URL https://linkinghub.elsevier.com/retrieve/pii/S2352152X23002220.

[14] Z.A. Qureshi, S.A.B. Al-Omari, E. Elnajjar, O. Al-Ketan, R.A. Al-Rub, Using triply periodic minimal surfaces (TPMS)-based metal foams structures as skeleton for metal-foam-PCM composites for thermal energy storage and energy management applications, Int. Commun. Heat Mass Transfer 124 (2021) 105265, http://dx.doi.org/10.1016/j.icheatmasstransfer.2021.105265, URL https://linkinghub.elsevier.com/retrieve/pii/S0735193321001597.

[15] S. Catchpole-Smith, R. Sélo, A. Davis, I. Ashcroft, C. Tuck, A. Clare, Thermal conductivity of TPMS lattice structures manufactured via laser powder bed fusion, Addit. Manuf. 30 (2019) 100846, http://dx.doi.org/10.1016/j.addma.2019.100846, URL https://linkinghub.elsevier.com/retrieve/pii/S2214860419307559.

[16] K. Swaminathan Gopalan, V. Eswaran, Numerical investigation of thermal performance of PCM based heat sink using structured porous media as thermal conductivity enhancers, Int. J. Therm. Sci. 104 (2016) 266–280, http://dx.doi.org/10.1016/j.ijthermalsci.2016.01.008, URL https://linkinghub.elsevier.com/retrieve/pii/S1290072916000168.

[17] M. Arqam, L.S. Raffa, S. Spisiak, L. Clemon, Z. Luo, M. Ryall, M.S. Islam, N.S. Bennett, Computational and experimental analysis of a novel triply periodic minimal surface heat sink with phase change material, J. Energy Storage 117 (2025) 116121, http://dx.doi.org/10.1016/j.est.2025.116121, URL https://linkinghub.elsevier.com/retrieve/pii/S2352152X25008345.

[18] L. Sueza Raffa, M. Ryall, N.S. Bennett, L. Clemon, Experimental investigation of the performance of a phase change material thermal management module under vacuum and atmospheric pressure conditions, Int. J. Heat Mass Transfer 236 (2025) 126384, http://dx.doi.org/10.1016/j.ijheatmasstransfer.2024.126384, URL https://linkinghub.elsevier.com/retrieve/pii/S0017931024012134.

[19] C.R. Raj, S. Suresh, R. Bhavsar, V.K. Singh, K.A. Govind, Influence of fin configurations in the heat transfer effectiveness of solid solid PCM based thermal control module for satellite avionics: Numerical simulations, J. Energy Storage 29 (2020) 101332, http://dx.doi.org/10.1016/j.est.2020.101332, URL https://linkinghub.elsevier.com/retrieve/pii/S2352152X19315865.

[20] A.M. Elshaer, A. Soliman, M. Kassab, S. Mori, A. Hawwash, Numerical study about thermal performance evaluation of PCM and PCM/fins composite-based thermal control module at microgravity conditions, Int. J. Thermofluids 20 (2023) 100419, http://dx.doi.org/10.1016/j.ijft.2023.100419, URL https://linkinghub.elsevier.com/retrieve/pii/S2666202723001350.

[21] B. İzgi, Effect of fins on melting of phase change material in a closed vertical cylinder under microgravity, Appl. Therm. Eng. 220 (2023) 119703, http://dx.doi.org/10.1016/j.applthermaleng.2022.119703, URL https://linkinghub.elsevier.com/retrieve/pii/S1359431122016337.

[22] S. Wang, X. Hou, J. Yin, Y. Xing, Z. Wang, Comparative study of the thermal enhancement for spacecraft PCM thermal energy storage units, Aerospace 9 (11) (2022) 705, http://dx.doi.org/10.3390/aerospace9110705, URL https://www.mdpi.com/2226-4310/9/11/705.

[23] Y. Guo, H. Yang, G. Lin, H. Jin, X. Shen, J. He, J. Miao, Thermal performance of a 3D printed lattice-structure heat sink packaging phase change material, Chin. J. Aeronaut. 34 (5) (2021) 373–385, http://dx.doi.org/10.1016/j.cja.2020.07.033, URL https://linkinghub.elsevier.com/retrieve/pii/S1000936120303551.

[24] R. Baby, C. Balaji, Experimental investigations on thermal performance enhancement and effect of orientation on porous matrix filled PCM based heat sink, Int. Commun. Heat Mass Transfer 46 (2013) 27–30, http://dx.doi.org/10.1016/j.icheatmasstransfer.2013.05.018, URL https://linkinghub.elsevier.com/retrieve/pii/S0735193313001140.

[25] S. Fok, W. Shen, F. Tan, Cooling of portable hand-held electronic devices using phase change materials in finned heat sinks, Int. J. Therm. Sci. 49 (1) (2010) 109–117, http://dx.doi.org/10.1016/j.ijthermalsci.2009.06.011, URL https://linkinghub.elsevier.com/retrieve/pii/S1290072909001471.

[26] B.M. Diaconu, M. Cruceru, L. Anghelescu, Phase change materials in space systems. Fundamental applications, materials and special requirements – A review, Acta Astronaut. 216 (2024) 163–213, http://dx.doi.org/10.1016/j.actaastro.2023.12.040, URL https://linkinghub.elsevier.com/retrieve/pii/S0094576523006707.

[27] M. Arqam, L.S. Raffa, M. Ryall, M.S. Islam, Numerical investigation of metal lattice heat sink geometries under the influence of phase change materials, J. Energy Storage 132 (2025) 117784, http://dx.doi.org/10.1016/j.est.2025.117784.

[28] M. Arqam, L.S. Raffa, L. Clemon, M.S. Islam, M. Ryall, N.S. Bennett, Numerical and experimental investigation of a phase change material radial fin heat sink for electronics cooling, J. Energy Storage 98 (2024) 113113, http://dx.doi.org/10.1016/j.est.2024.113113, URL https://linkinghub.elsevier.com/retrieve/pii/S2352152X24026999.

[29] Sigma-aldrich product specification: Paraffin wax 327204, 2024, URL https://www.sigmaaldrich.com/specification-sheets/325/952/327204-BULK_____ALDRICH_.pdf.

[30] S. Corpino, M. Caldera, F. Nichele, M. Masoero, N. Viola, Thermal design and analysis of a nanosatellite in low earth orbit, Acta Astronaut. 115 (2015) 247–261, http://dx.doi.org/10.1016/j.actaastro.2015.05.012, URL https://linkinghub.elsevier.com/retrieve/pii/S0094576515001940.

[31] S. Isaacs, D.A. Arias, G. Shoukas, Development of a lightweight and low-cost 3D-printed aluminum and PCM panel for thermal management of CubeSat applications, in: 47th International Conference on Environmental Systems, 2017.

[32] L. Sueza Raffa, M. Ryall, I.H. Cairns, N.S. Bennett, L.M. Clemon, Investigating the performance of a heat sink for satellite avionics thermal management: From ground-level testing to space-like conditions, Int. J. Heat Mass Transfer 248 (2025) 127139, http://dx.doi.org/10.1016/j.ijheatmasstransfer.2025.127139, URL https://www.ssrn.com/abstract=5164822.

[33] A. Arshad, M. Ibrahim Alabdullatif, M. Jabbal, Y. Yan, Towards the thermal management of electronic devices: A parametric investigation of finned heat sink filled with PCM, Int. Commun. Heat Mass Transfer 129 (2021) 105643, http://dx.doi.org/10.1016/j.icheatmasstransfer.2021.105643, URL https://linkinghub.elsevier.com/retrieve/pii/S0735193321005364.

[34] K. Nayak, S. Saha, K. Srinivasan, P. Dutta, A numerical model for heat sinks with phase change materials and thermal conductivity enhancers, Int. J. Heat Mass Transfer 49 (11–12) (2006) 1833–1844, http://dx.doi.org/10.1016/j.ijheatmasstransfer.2005.10.039, URL https://linkinghub.elsevier.com/retrieve/pii/S0017931005006824.

[35] J. Xie, K.F. Choo, J. Xiang, H.M. Lee, Characterization of natural convection in a PCM-based heat sink with novel conductive structures, Int. Commun. Heat Mass Transfer 108 (2019) 104306, http://dx.doi.org/10.1016/j.icheatmasstransfer.2019.104306, URL https://linkinghub.elsevier.com/retrieve/pii/S0735193319301721.